

Anatomy-aware and acquisition-agnostic joint registration with SynthMorph

Malte Hoffmann^{a-d,*}, Andrew Hoopes^{a-b,e},
Douglas N. Greve^{a-c}, Bruce Fischl^{a-e,1}, Adrian V. Dalca^{a-c,e,1}

^a Athinoula A. Martinos Center for Biomedical Imaging, Charlestown, MA, USA

^b Department of Radiology, Massachusetts General Hospital, Boston, MA, USA

^c Department of Radiology, Harvard Medical School, Boston, MA, USA

^d Harvard-MIT Health Sciences and Technology, Massachusetts Institute of Technology, Cambridge, MA, USA

^e Computer Science & Artificial Intelligence Laboratory, Massachusetts Institute of Technology, Cambridge, MA, USA

* Corresponding author, mhoffmann@mgh.harvard.edu. ¹ These authors contributed equally.

Abstract Affine image registration is a cornerstone of medical-image analysis. While classical algorithms can achieve excellent accuracy, they solve a time-consuming optimization for every image pair. Deep-learning (DL) methods learn a function that maps an image pair to an output transform. Evaluating the function is fast, but capturing large transforms can be challenging, and networks tend to struggle if a test-image characteristic shifts from the training domain, such as resolution. Most affine methods are agnostic to the anatomy the user wishes to align, meaning the registration will be inaccurate if algorithms consider all structures in the image. We address these shortcomings with SynthMorph, a fast, robust, and easy-to-use DL tool for joint affine-deformable registration of any brain image without preprocessing, right off the MRI scanner. First, we leverage a strategy to train networks with wildly varying images synthesized from label maps, yielding robust performance across acquisition specifics unseen at training. Second, we optimize the spatial overlap of select anatomical labels. This enables networks to distinguish anatomy of interest from irrelevant structures, removing the need for preprocessing that excludes content which would impinge on anatomy-specific registration. Third, we combine the affine model with a deformable hypernetwork that lets users choose the optimal deformation-field regularity for their specific data, at registration time, in a fraction of the time required by classical methods. This framework is applicable to learning anatomy-aware, acquisition-agnostic registration of any anatomy with any architecture, as long as label maps are available for training. We rigorously analyze how competing architectures learn affine transforms and compare state-of-the-art registration tools across an extremely diverse set of neuroimaging data, aiming to truly capture the behavior of methods in the real world. SynthMorph demonstrates consistent and improved accuracy and is available at <https://w3id.org/synthmorph>, as a single complete end-to-end solution for registration of brain MRI.

Keywords Affine registration, deformable registration, deep learning, hypernetwork, domain shift, neuroimaging.

1 Introduction

Image registration is an essential component of medical image processing and analysis that estimates a mapping from the space of the anatomy in one image to the space of another image (Cox, 1996; Fischl et al., 2002, 2004; Jenkinson et al., 2012; Tustison et al., 2013). Such transforms generally include an affine component accounting for global orientation such as different head positions, which are typically not of clinical interest. Transforms often include a deformable component that may represent anatomically meaningful differences in geometry (Hajnal and Hill, 2001). Many techniques analyze these further, for example voxel-based morphometry (Ashburner and Friston, 2000; Whitwell, 2009).

Iterative registration has been extensively studied, and the available methods can achieve excellent accuracy both within and across magnetic resonance imaging (MRI) contrasts (Ashburner, 2007; Cox and Jesmanowicz, 1999;

Friston et al., 1995; Jiang et al., 1995; Lorenzi et al., 2013; Rohr et al., 2001; Rueckert et al., 1999). Approaches differ in how they measure image similarity and the strategy chosen to optimize it, but the fundamental algorithm is the same: fit a set of parameters modeling the spatial transformation between an image pair by iteratively minimizing a dissimilarity metric. While classical deformable registration can take tens of minutes to several hours, affine registration optimizes only a handful of parameters and is generally faster (Hoffmann et al., 2015; Jenkinson and Smith, 2001; Modat et al., 2014; Reuter et al., 2010). For these reasons, classical affine methods are still widely used both within analysis pipelines and also for more specialized applications such as correcting head motion during image acquisition (Gallichan et al., 2016; Thesen et al., 2000; Tisdall et al., 2012). However, these approaches solve an optimization problem for every new image pair, which is inefficient: depending on the algorithm, affine registration of higher-resolution struc-

tural MRI, for example, can easily take 5-10 minutes (Table 3). Further, iterative pipelines can be laborious to use. The user typically has to tailor the optimization strategy and choose a similarity metric appropriate for the image appearance (Pustina and Cook, 2017). Often, images require preprocessing, including intensity normalization or removal of structures that the registration should exclude. These shortcomings have motivated work on deep-learning (DL) based registration.

Recent advances in DL have enabled registration with unprecedented efficiency and accuracy (Balakrishnan et al., 2019; Dalca et al., 2018; Eppenhof and Pluim, 2019; Krebs et al., 2017; Li and Fan, 2017; Rohé et al., 2017; Sokooti et al., 2017; Yang et al., 2016, 2017). In contrast to classical approaches, DL models learn a function that maps an input registration pair to an output transform. While evaluating this function on a new pair of images is fast, most existing DL methods focus on the deformable component. Affine registration of the input images is often assumed (Balakrishnan et al., 2019; de Vos et al., 2017) or incorporated *ad hoc*, and thus given less attention than deformable registration (De Vos et al., 2019; Hu et al., 2018; Mok and Chung, 2022; Zhao et al., 2019b,d). Although state-of-the-art deformable algorithms are capable of compensating for sub-optimal affine alignment to some extent, they cannot always fully recover the lost accuracy, as the experiment of Section 4.6 will show. Further, any inaccuracy in the affine transform will make it harder to interpret the deformable component (Bookstein, 2001; Ou et al., 2014), which will now include an undesired affine residual.

The learning-based models encompassing both affine and deformable components usually do not consider network generalization to modality variation (De Vos et al., 2019; Shen et al., 2019; Zhao et al., 2019b,d; Zhu et al., 2021). That is, networks trained on one type of data, such as T1-weighted (T1w) MRI, tend to inaccurately register other types of data, such as T2-weighted (T2w) scans. Even for similar MRI contrast, the domain shift caused by different noise or smoothness levels alone has the potential to reduce accuracy at test time. In contrast, learning frameworks capitalizing on generalization techniques and domain adaptation often do not incorporate the fundamental affine transform (Chen et al., 2017; Iglesias et al., 2013; Qin et al., 2019; Tanner et al., 2018).

A separate challenge for affine registration consists in accurately aligning specific anatomy of interest in the image while ignoring irrelevant content. Any undesired structure that moves independently or deforms non-linearly will reduce the accuracy of the anatomy-specific transform unless an algorithm has the ability to ignore it. For example, neck and tongue tissue can confuse rigid brain registration when they deform non-rigidly (Andrade et al., 2018; Fein et al., 2006; Fischmeister et al., 2013; Hoffmann et al., 2020). Identifying a suitable architecture for affine registration and formulating the problem in a differentiable manner will enable embedding and jointly

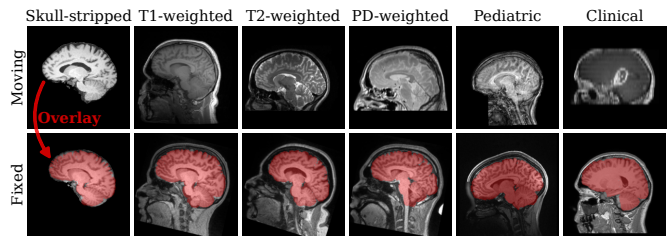


Figure 1. Representative examples of anatomy-aware SynthMorph affine 3D registration showing the moving brain transformed onto the fixed brain (red overlay). Trained with highly variable synthetic data, SynthMorph generalizes across a diverse array of real-world contrasts, resolutions, and subject populations without any preprocessing.

learning affine registration with other tasks, for example creating conditional atlases representing a subject population, from non-aligned input images (Dalca et al., 2019a; Ding and Niethammer, 2022; Sinclair et al., 2022).

1.1 Contribution

In this work we present a single, easy-to-use DL tool for end-to-end affine and deformable brain registration for images right off the MRI scanner, without preprocessing (Figure 1). The tool performs robustly across MRI contrasts, intensity scales, and resolutions. We address the domain dependency and anatomical non-specificity of affine registration: while invariance to acquisition specifics will enable networks to generalize to new image types without retraining, our anatomy-specific training strategy alleviates the need for pre-processing segmentation steps that remove image content which would distract a majority of registration methods—as Section 4.5 will show for the example of skull-stripping (Eskildsen et al., 2012; Hoopes et al., 2022b; Iglesias et al., 2011; Salehi et al., 2017; Smith, 2002).

Our work builds on ideas from DL-based registration, affine registration, and a recent synthesis-based training strategy that promotes data independence by exposing networks to arbitrary image contrasts (Billot et al., 2020; Hoffmann et al., 2021a; Hoopes et al., 2022b).

First, we rigorously analyze three fundamental network architectures in Section 4.4, to provide insight into how DL models learn and best represent the affine component. Second, we select an optimized architecture and train the network with *synthetic* data only, making it robust across a landscape of acquired image types without exposing it to any real images during training. Third, we combine the affine model with a deformable hypernetwork to create an end-to-end registration tool, enabling users to choose a regularization strength that is optimal for their own data *without* retraining and in a fraction of the time required by classical methods. Fourth, we test the resulting model across a very diverse set of images, aiming to truly capture the diversity of real-world data. We compare its performance against popular affine and deformable toolboxes in Sections 4.5 and 4.6, respectively, to thoroughly assess

the registration accuracy users can achieve with off-the-shelf implementations on images unseen at training. We freely distribute our code and stand-alone tool, SynthMorph, at <https://w3id.org/synthmorph> and within the upcoming FreeSurfer release (Fischl, 2012).

2 Related work

There is substantial work on medical image registration. While this section provides an overview of successful and widely adopted strategies, more in-depth review articles are available (Fu et al., 2020; Oliveira and Tavares, 2014; Wyawahare et al., 2009).

2.1 Classical registration

Classical registration is driven by an objective function, which measures similarity in appearance between the moving and the fixed image. A simple and effective choice for images of the same contrast is the mean squared error (MSE). Normalized cross-correlation (NCC) is also widely used, because it provides excellent accuracy independent of the intensity scale (Avants et al., 2008). Registration of images across contrasts or modalities generally employs objective functions such as normalized mutual information (NMI) (Maes et al., 1997; Wells III et al., 1996) or the correlation ratio (Roche et al., 1998), as these do not assume similar appearance of the input images. Another class of classical registration methods uses metrics based on patch similarity (Glocker et al., 2008, 2011; Ou et al., 2011), which can outperform simpler metrics across modalities (Hoffmann et al., 2021a).

To improve computational efficiency and avoid local minima, many classical techniques perform multi-resolution searches (Hellier et al., 2001; Nestares and Heeger, 2000). First, this strategy coarsely aligns smoothed downsampled versions of the input images. This initial solution is subsequently refined at higher resolutions until the original images align precisely (Avants et al., 2011; Modat et al., 2014; Reuter et al., 2010). Additionally, an initial grid search over a set of rotation parameters can help constrain this scale-space approach to a neighborhood around the global optimum (Jenkinson and Smith, 2001; Jenkinson et al., 2012).

Instead of optimizing image similarity, another registration paradigm detects landmarks and matches these across the images (Myronenko and Song, 2010). Early work relied on user assistance to identify fiducials (Besl and McKay, 1992; Meyer et al., 1995). More recent computer-vision approaches automatically extract features (Machado et al., 2018; Toews and Wells III, 2013), for example from entropy (Wachinger and Navab, 2010, 2012) or difference-of-Gaussians images (Lowe, 2004; Rister et al., 2017; Wachinger et al., 2018). The performance of this strategy depends on the invariance of landmarks across viewpoints and intensity scales (Matas et al., 2004).

2.2 Deep-learning registration

Analogous to classical registration, unsupervised deformable DL methods fit the parameters of a deep neural network by optimizing a loss function that measures image similarity—but across many image pairs (Balakrishnan et al., 2019; Dalca et al., 2019b; De Vos et al., 2019; Guo, 2019; Hoffmann et al., 2021a; Krebs et al., 2019). In contrast, supervised DL strategies (Eppenhof and Pluim, 2019; Krebs et al., 2017; Rohé et al., 2017; Sokooti et al., 2017; Yang et al., 2016, 2017) train a network to reproduce ground-truth transforms, for example obtained with classical tools, and tend to underperform relative to their unsupervised counterparts (Hoffmann et al., 2021a; Young et al., 2022), although warping features at the end of each U-Net (Ronneberger et al., 2015) level can close the performance gap (Young et al., 2022).

2.2.1 Affine deep-learning registration

Similar to the deformable case, affine registration strategies can be supervised or unsupervised but require a different network architecture. A straightforward option combines a convolutional encoder with a fully connected (FC) layer to predict the parameters of an affine transform in one shot (Shen et al., 2019; Zhao et al., 2019b,d; Zhu et al., 2021). A series of convolutional blocks successively halve the image dimension, such that the output of the final convolution has substantially fewer voxels than the input images. This facilitates the use of the FC layer with the desired number of output units, preventing the number of network parameters from becoming intractably large. Networks typically concatenate the input images before passing them through the encoder. To benefit from weight sharing, twin networks pass the fixed and moving images separately through the same encoder and connect their outputs at the end (Chen et al., 2021; De Vos et al., 2019).

As affine transforms have a global effect on the image, some architectures replace the locally operating convolutional layers with vision transformers (Dosovitskiy et al., 2020; Mok and Chung, 2022). These models subdivide their inputs into patch embeddings and pass them through the transformer, before a multi-layer perceptron (MLP) outputs a transformation matrix. Multiple such modules in series can successively refine the affine transform if each module applies its output transform to the moving image before passing it onto the next stage (Mok and Chung, 2022). Composition of the transforms from each step produces the final output matrix.

Another affine DL strategy (Moyer et al., 2021; Yu et al., 2022) derives an affine transform without requiring MLP or FC layers, similar to the classical feature extraction and matching approach (Section 2.1). This method separately passes the moving and the fixed image through a convolutional encoder to detect two corresponding sets of feature maps. Computing the barycenter of each feature map yields moving and fixed point clouds, and a

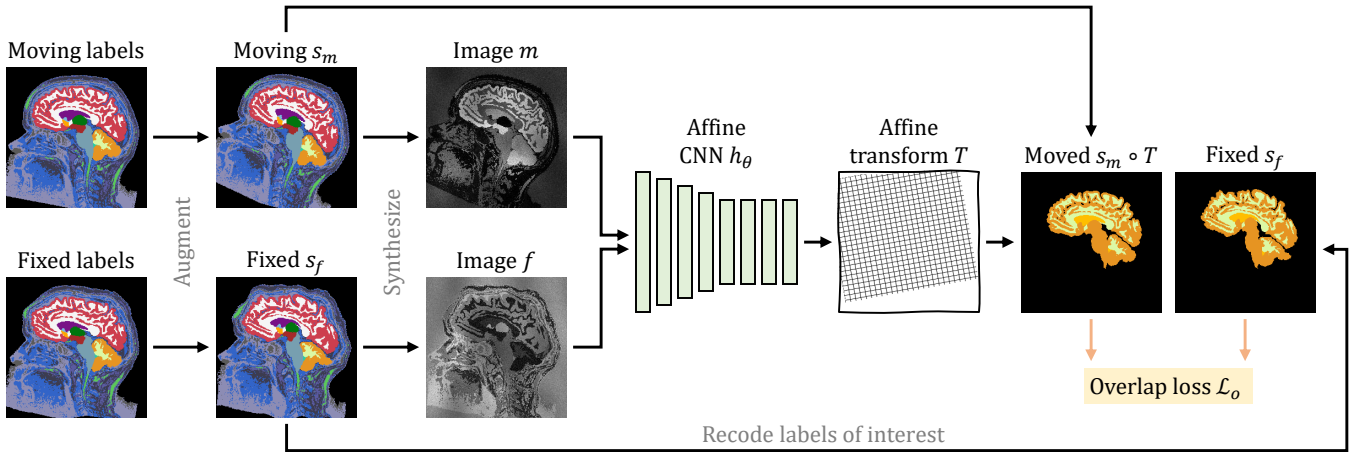


Figure 2. Training strategy for affine registration. At each iteration, we augment a pair of moving and fixed label maps $\{s_m, s_f\}$ and synthesize images $\{m, f\}$ from them. The network h_θ predicts an affine transform T that we compute the moved label map $s_m \circ T$ from. Loss \mathcal{L}_o recodes the labels in $\{s_m, s_f\}$ to optimize the overlap of select anatomy of interest only, such as WM, GM, and CSF. We emphasize the wide applicability of this strategy to learning anatomy-aware and acquisition-agnostic registration of any anatomy and with any network architecture, as long as label maps are available for training.

least-squares (LS) fit provides a transform aligning them. The approach is robust across large transforms (Yu et al., 2022), while removing the FC layer alleviates the dependency of the architecture on a specific image size.

In this work, we will thoroughly test these fundamental DL architectures and extend them to build an end-to-end solution for joint affine and deformable registration that is aware of the anatomy of interest.

2.3 Robustness and anatomical specificity

Indiscriminate registration of images as a whole can limit the accurate alignment of specific substructures, such as the brain in whole-head MRI. One group of classical methods avoids this problem by down-weighting image regions that cannot be mapped accurately with the chosen transformation model, for example using an iteratively re-weighted LS algorithm (Billings et al., 2015; Gelfand et al., 2005; Modat et al., 2014; Nestares and Heeger, 2000; Puglisi and Battiato, 2011; Reuter et al., 2010). Few approaches focus on specific anatomical features, for example by restricting the registration to regions of an atlas with high prior probability for belonging to a particular tissue class (Fischl et al., 2002). The affine registration tools most commonly used in neuroimage analysis (Cox, 1996; Friston et al., 1995; Jenkinson and Smith, 2001; Modat et al., 2014) instead expect—and require—that distracting image content be removed from the input data as a preprocessing step for optimal performance (Es-kildsen et al., 2012; Iglesias et al., 2011; Klein et al., 2009; Smith, 2002). Similarly, many DL registration algorithms assume intensity-normalized and skull-stripped input images (Balakrishnan et al., 2019; Yu et al., 2022; Zhao et al., 2019d), preventing their applicability to diverse unprocessed data.

2.4 Domain generalizability

The adaptability of neural networks to out-of-distribution data generally presents a challenge to their deployment (Sun et al., 2016; Wang and Deng, 2018). Mitigation strategies include augmenting the variability of the training distribution, for example by adding random noise or applying geometric transforms (Chaitanya et al., 2019; Perez and Wang, 2017; Shorten and Khoshgoftaar, 2019; Zhao et al., 2019a). Transfer learning adapts a trained network to a new domain by fine-tuning deeper layers on the target distribution (Kamnitsas et al., 2017; Zhuang et al., 2020). These methods require training data from the target domain. By contrast, within medical imaging, a recent strategy synthesizes wildly variable training images to promote data independence. The resulting networks generalize beyond dataset specifics and perform with high accuracy on tasks including segmentation (Billot et al., 2020), deformable registration (Hoffmann et al., 2021a), and skull-stripping (Hoopes et al., 2022b). We build on this technology to achieve end-to-end registration incorporating the affine component.

3 Method

3.1 Background

3.1.1 Learning-based registration

Let m be a moving and f a fixed image in N -dimensional (ND) space. We train a deep neural network h_θ with learnable parameters θ to predict a global transform $T_\theta : \Omega \rightarrow \mathbb{R}^N$ that maps the spatial domain Ω of f onto m .

The transform $T_\theta = h_\theta(m, f)$ is a matrix

$$T_\theta = \left(\begin{array}{c|c} A_\theta & v_\theta \\ \hline 0 & 1 \end{array} \right) = \left(\begin{array}{c} t_\theta \\ \hline 0 \dots 0 \quad 1 \end{array} \right), \quad (1)$$

where matrix $A_\theta \in \mathbb{R}^{N \times N}$ represents rotation, scaling, and shear, and $v_\theta \in \mathbb{R}^{N \times 1}$ is a vector of translational shifts, such that $t_\theta \in \mathbb{R}^{N \times (N+1)}$. We fit the network weights θ to training set \mathcal{D} subject to

$$\hat{\theta} = \arg \min_{\theta} \mathbb{E}_{(m, f) \in \mathcal{D}^2} \left[\mathcal{L}_s(m \circ h_\theta(m, f), f) \right], \quad (2)$$

where the loss \mathcal{L}_s measures the similarity in appearance between two input images, and $m \circ T_\theta$ means m transformed by $T_\theta = h_\theta(m, f)$.

3.1.2 Synthesis-based training

A recent strategy (Billot et al., 2020; Hoffmann et al., 2021a,b, 2023; Hoopes et al., 2022b) achieves robustness to preprocessing and acquisition specifics by training networks exclusively with synthetic images generated from label maps. From a set of label maps $\{s_m, s_f\}$, a generative model synthesizes corresponding wildly variable images $\{m, f\}$ as network inputs. Instead of image similarity, the strategy optimizes spatial label overlap with a (soft) Dice-based loss \mathcal{L}_o (Milletari et al., 2016), completely independent of image appearance:

$$\mathcal{L}_o(\theta, s_m, s_f) = -\frac{2}{|J|} \sum_{\substack{j \in J \\ x \in \Omega}} \frac{(s_m|_j \circ T_\theta)(x) \times s_f|_j(x)}{(s_m|_j \circ T_\theta)(x) + s_f|_j(x)}, \quad (3)$$

where $s|_j$ represents the one-hot encoded label $j \in J$ of label map s defined at the voxel locations $x \in \Omega$ in the discrete spatial domain Ω of f .

The generative model requires only a few input label maps to produce a stream of diverse training images, helping the task network accurately generalize to real medical images of any contrast at test time, which it can then register without needing label maps.

3.2 Anatomy-aware joint registration

As we build on our recent work on deformable registration, SynthMorph (Hoffmann et al., 2021a), here we only provide a high-level overview and focus on what is new for affine and joint affine-deformable registration. Figure 2 illustrates our learning setup for affine registration.

3.2.1 Label maps

Every training iteration, we draw a pair of moving and fixed brain segmentations. We apply random spatial transformations to each of them to augment the range of

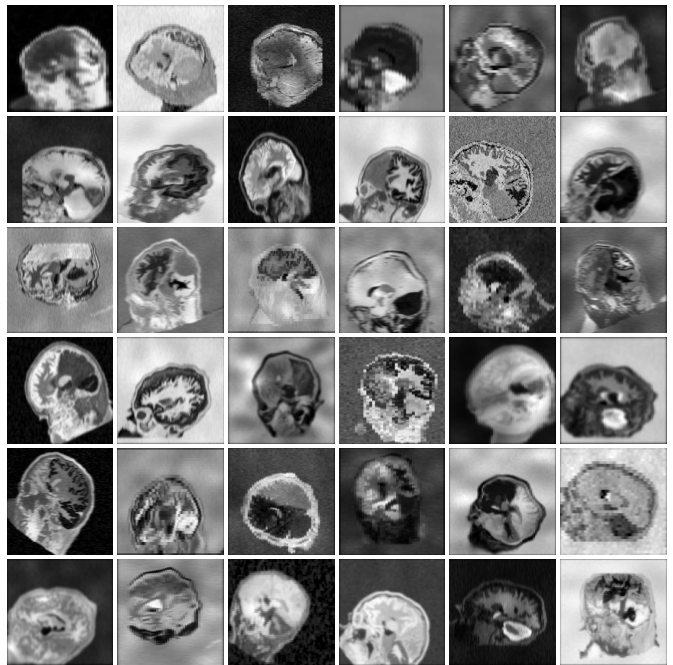


Figure 3. Synthetic 3D training data with arbitrary contrast, resolution, and artifact level, generated from brain label maps. The image characteristics exceed the realistic range to promote network generalization across acquisition protocols. All examples are based on the same label map. In practice, we use several different subjects.

head orientations and anatomical variability in the training set. Specifically, we construct an affine matrix from random translation, rotation, scaling, and shear as detailed in Appendix A. We compose the affine transform with a randomly sampled and randomly smoothed deformation field (Hoffmann et al., 2021a) and apply the composite transform in a single interpolation step. Finally, we simulate acquisitions with a partial field of view (FOV) by randomly cropping the label map content, yielding label maps $\{s_m, s_f\}$.

3.2.2 Anatomical specificity

Let K be the complete set of labels in $\{s_m, s_f\}$. To encourage networks to register specific anatomy while ignoring irrelevant image content, we propose to recode $\{s_m, s_f\}$ such that the label maps include only a subset of labels $J \subset K$. For brain-specific registration, J consists of individual brain structures in the deformable case or larger tissue classes in the affine case. At training, the loss \mathcal{L} optimizes only the overlap of J , whereas we synthesize images from the complete set of labels K , providing rich image content outside the brain as illustrated in Figure 2.

3.2.3 Image synthesis

Given label map s_m , we generate image m with random contrast, noise, and artifact corruption (and similarly f from s_f). Following SynthMorph, we first sample a mean intensity for each label $j \in K$ in s_m and assign this value

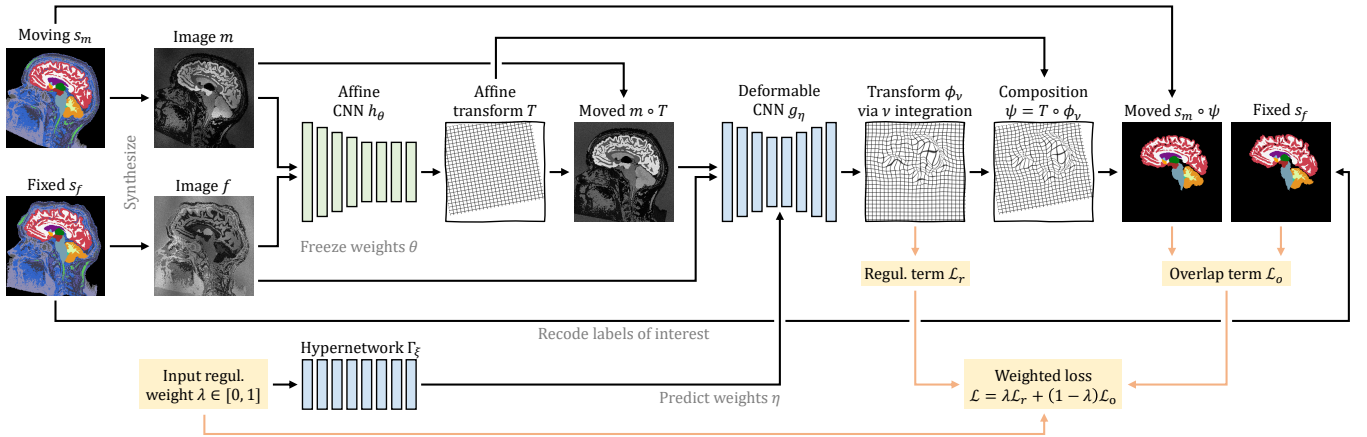


Figure 4. Training strategy for joint registration. As in Figure 2, network h_θ predicts an affine transform T between moving and fixed images $\{m, f\}$ synthesized from label maps $\{s_m, s_f\}$. Hypernetwork Γ_ξ takes the regularization weight λ as input and outputs the parameters $\eta = \Gamma_\xi(\lambda)$ of network g_η . The moved image $m \circ T$ and f are inputs to g_η , which predicts a diffeomorphic warp field ϕ . We form the joint transform $\psi = T \circ \phi$ by composition and compute the moved label map $s_m \circ \psi$. Loss \mathcal{L}_o recodes the labels of $\{s_m, s_f\}$ to optimize the overlap of select anatomy of interest—in this case brain labels only. We emphasize the wide applicability of this strategy to learning anatomy-aware and acquisition-agnostic registration of any anatomy and with any network architecture, as long as label maps are available for training.

to all voxels associated with label j . Second, we corrupt m by randomly applying additive Gaussian noise, anisotropic Gaussian blurring, a multiplicative spatial intensity bias field, intensity exponentiation with a global parameter, and downsampling along randomized axes. In aggregate, these steps produce widely varying intensity distributions within each anatomical label (Figure 3).

3.2.4 Generation hyperparameters

We choose the affine augmentation range such that it encompasses real-world transforms. Figure C.1 (Appendix C) shows the distribution of affine transformation parameters measured across public datasets. We adapt all other values from prior work, which thoroughly analyzed their impact on registration accuracy (Hoffmann et al., 2021a): Table B.1 (Appendix B) lists hyperparameters for label-map augmentation and image synthesis.

3.2.5 Joint registration

For joint registration, we combine the affine model h_θ with the deformable SynthMorph architecture. Let g_η be a convolutional neural network model with parameters η that predicts the warp field $\phi_\eta = g_\eta(m, f)$. Usually, approaches to learning deformable registration would directly fit weights η by optimizing a loss of the form

$$\mathcal{L}(\eta, s_m, s_f) = (1 - \lambda)\mathcal{L}_o(\phi_\eta, s_m, s_f) + \lambda\mathcal{L}_r(\phi_\eta), \quad (4)$$

where \mathcal{L}_o quantifies label overlap as before, \mathcal{L}_r is a regularization term that encourages smooth warps, and the hyperparameter $\lambda \in [0, 1]$ controls the weighting of both terms.

Because directly fitting weights η yields an inflexible network g_η predicting warps of fixed regularity, we parameterize η using a hypernetwork approach. Let Γ_ξ be

a neural network with trainable parameters ξ . Following our prior work (Hoopes et al., 2022a), hypernetwork Γ_ξ takes the regularization weight λ as input and outputs the weights $\eta = \Gamma_\xi(\lambda)$ of the deformable task network g_η . Consequently, g_η has no learnable parameters in our setup—its convolutional kernels η can flexibly adapt in response to the value λ takes at test time.

As shown in Figure 4, for joint registration we move image m based on the affine transform $T_\theta = h_\theta(m, f)$, and g_η predicts the warp field $\phi_\xi = g_\eta(m \circ T_\theta, f)$ using kernels $\eta = \Gamma_\xi(\lambda)$ specific to input λ . The total transform is $\psi_{\theta\xi} = T_\theta \circ \phi_\xi$, while the loss of Equation (4) becomes

$$\mathcal{L}(\lambda, \theta, \xi, s_m, s_f) = (1 - \lambda)\mathcal{L}_o(\psi_{\theta\xi}, s_m, s_f) + \lambda\mathcal{L}_r(\phi_\xi), \quad (5)$$

We choose $\mathcal{L}_r(\phi) = \|\nabla u\|_2$, where u is the displacement of the deformation $\phi = id + u$, and id is the identity field.

3.2.6 Overlap loss

In this work, we replace the Dice-based overlap loss term of Equation (3) with a simpler term (Heinrich, 2019; Wang et al., 2021) that measures MSE between one-hot encoded labels $s|_j$,

$$\mathcal{L}_o(\theta, s_m, s_f) = \frac{1}{|\Omega|} \sum_{\substack{j \in J \\ x \in \Omega}} \left[(s_m|_j \circ T_\theta)(x) - s_f|_j(x) \right]^2 \quad (6)$$

where we replace weights θ with $\{\theta, \xi\}$ and transform T_θ with $\psi_{\theta\xi}$ for joint registration. MSE is sensitive to the proportionate contribution of each label $j \in J$ to overall alignment, whereas Equation (3) normalizes the contribution of each label by its respective size. As a result, the MSE loss term discourages the optimization to disproportionately focus on aligning smaller structures, which we find favorable for warp regularity at structure boundaries.

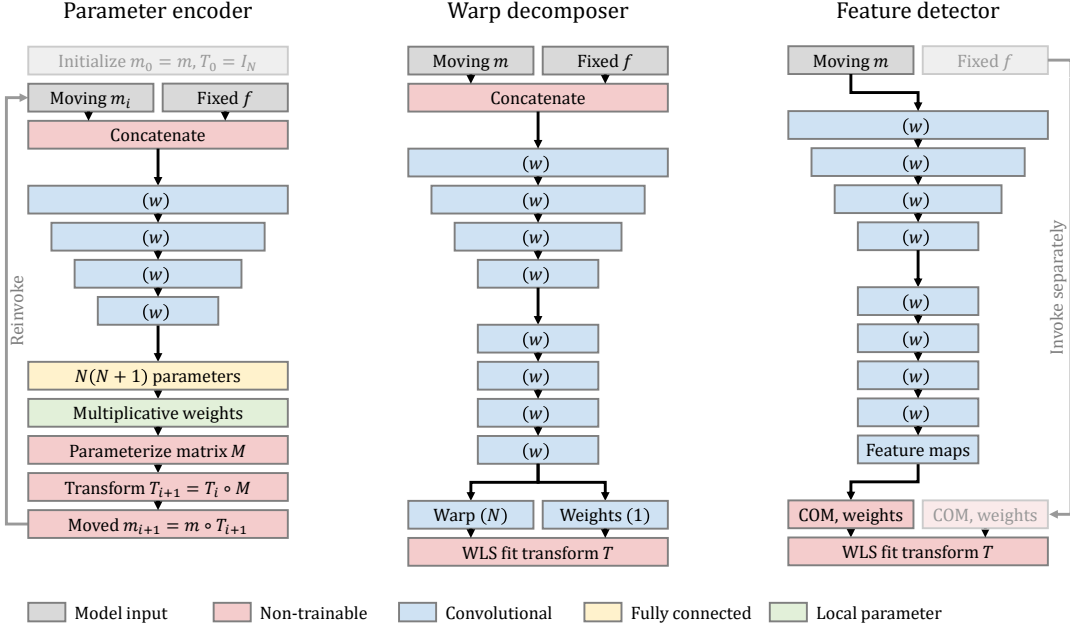


Figure 5. Affine registration architectures. A recurrent Encoder estimates refinements to the current transform T_i from moved image $m_i = m \circ T_i$ and fixed image f . Decomposer predicts a one-shot displacement field (no activation) with corresponding voxel weights (ReLU), that we decompose in a weighted least-squares (WLS) sense to estimate affine transform T . Detector outputs ReLU-activated feature maps for a single image. We compute their centers of mass (COM) and weights separately for m and f , to fit a transform T that aligns these point sets. Parentheses specify filter numbers. We LeakyReLU-activate the output of unnamed convolutional blocks (param. $\alpha = 0.2$). Stacked convolutional blocks of decreasing size indicate subsampling by a factor of 2 via max pooling following each activation.

3.3 Affine architectures

Estimating an affine transform T from a pair of medical images in ND requires reducing a large input space of the order of 100k–10M voxels to only $N(N+1)$ output parameters. We analyze three competing network architectures (Figure 5) that represent state-of-the-art methods (Balakrishnan et al., 2019; De Vos et al., 2019; Moyer et al., 2021; Shen et al., 2019; Yu et al., 2022; Zhu et al., 2021).

3.3.1 Parameter encoder

We first build on networks combining a convolutional encoder with an FC layer (Shen et al., 2019; Zhu et al., 2021) whose $N(N+1)$ output units we interpret as parameters for translation, rotation, scale, and shear. We refer to a cascade of C such subnetworks h_i , with $i \in \{1, 2, \dots, C\}$ as “Encoder”. Each h_i outputs a matrix constructed from the affine parameters as shown in Appendix A, to incrementally update the total transform. We obtain transform T_i by matrix multiplication after invoking subnetwork h_i ,

$$T_i = h_1(m_0, f) h_2(m_1, f) \cdots h_i(m_{i-1}, f) \quad (7)$$

where $m_i = m \circ T_i$ is the moving image transformed by T_i , and $T_0 = I_N$ is the identity matrix. As the subnetworks h_i are architecturally identical, weight sharing is possible, and we evaluate versions of the model with and without weights shared across cascades.

For balanced gradient steps, we complete each sub-network with a layer involving learnable local rescaling weights applied to the affine parameters before matrix construction.

3.3.2 Warp decomposer

We propose a second architecture building on deformable registration models (Balakrishnan et al., 2019; De Vos et al., 2019). “Decomposer” estimates a dense deformation field ϕ_θ with corresponding non-negative voxel weights κ_θ that we decompose into the affine output transform $T_\theta = h_\theta(m, f)$ and a (discarded) residual component δ_θ , i.e. $\phi_\theta = \delta_\theta \circ T_\theta$. The voxel weights κ_θ enable the network h_θ to focus the decomposition on the anatomy of interest. Both $(\phi_\theta, \kappa_\theta)$ are the output of a single fully convolutional network and thus benefit from weight sharing. We decompose ϕ_θ in a weighted least-squares (WLS) sense over the discrete spatial domain Ω of f , using the definition of t from Equation (1) as the submatrix of T that excludes the last row:

$$\hat{t}_\theta = \arg \min_t \sum_{x \in \Omega} \kappa_\theta(x) \|\phi_\theta(x)^\top - (x^\top \quad 1) t^\top\|^2, \quad (8)$$

where t^\top is the matrix transpose of t . Denoting $W = \text{diag}(\kappa_\theta)$, and by X and y the matrices whose corresponding rows are $(x^\top \quad 1)$ and $\phi_\theta(x)^\top$ for each $x \in \Omega$, respectively, the closed-form solution of Equation (8) is,

$$\hat{t}_\theta^\top = (X^\top W X)^{-1} X^\top W y. \quad (9)$$

3.3.3 Feature detector

Third, we extend a recent architecture (Moyer et al., 2021; Yu et al., 2022) that takes a single image as input and predicts a set of k non-negative spatial feature maps F_i with $i \in \{1, 2, \dots, k\}$, to support full affine transforms (Yu et al., 2022) and WLS (Moyer et al., 2021).

Following a series of convolutions, we compute the center of mass a_i and channel power $p_i|_m$ for each feature map $F_i|_m$ of the moving image,

$$a_i = p_i^{-1} \sum_{x \in \Omega} x F_i|_m(x), \quad p_i|_m = \sum_{x \in \Omega} F_i|_m(x), \quad (10)$$

and separately center of mass b_i with channel power $p_i|_f$ for each $F_i|_f$ of the fixed image. We interpret the sets $\{a_i\}$ and $\{b_i\}$ as corresponding moving and fixed point clouds. ‘‘Detector’’ refers to a network h_θ that returns the affine transform $t_\theta = h_\theta(m, f)$ aligning these point clouds subject to

$$\hat{t}_\theta = \arg \min_t \sum_{i=1}^k \epsilon_i \|a_i^\top - (b_i^\top \quad 1) t^\top\|^2, \quad (11)$$

where we define the normalized scalar weight ϵ_i as

$$\epsilon_i = p_i|_m \left(\sum_{j=1}^k p_j|_m \right)^{-1} p_i|_f \left(\sum_{j=1}^k p_j|_f \right)^{-1}. \quad (12)$$

Let X and y be matrices whose i^{th} rows are $(a_i^\top \quad 1)$ and b_i^\top , respectively. With $W = \text{diag}(\{\epsilon_i\})$, Equation (9) yields the closed-form solution \hat{t}_θ as above.

3.3.4 Implementation

Except for the final convolutions indicated in Figure 5, each affine model h_θ uses convolutional blocks with w filters; the network width w does not vary within a model. Unless stated otherwise, we activate the output of each block with LeakyReLU (parameter $\alpha = 0.2$) and down-sample by a factor of 2 using max pooling.

As in our prior work, the deformable model g_η implements a U-Net (Ronneberger et al., 2015) architecture of width $w = 256$ and integrates a stationary velocity field (SVF) ν to predict a diffeomorphism (Ashburner, 2007; Dalca et al., 2018). Hypermodel Γ_ξ is a simple feed-forward network with 4 ReLU-activated hidden FC layers that have 32 output units each.

All kernels are of size 3^N . For computational efficiency, our 3D models linearly down-sample the network inputs $\{m, f\}$ and loss inputs $\{s_m, s_f\}$ by a factor of 2. We min-max normalize input images such that their intensities fall in the interval $[0, 1]$. Affine coordinate transforms operate in a zero-centered index space, and we have Encoder predict rotation parameters in degrees. This parameterization ensures varying rotation angles has an effect of similar magnitude as translations in millimeters, at the scale of the brain, which we find helps networks converge faster. Appendix A includes further details.

3.3.5 Optimization

We fit model parameters with stochastic gradient descent using Adam (Kingma and Ba, 2014) over consecutive training strips S_i ($i \in \{1, 2, \dots\}$) of 10^6 batches each. At the beginning of each strip or in the event of divergence, we choose successively smaller learning rates from $l \in \{10^{-4}, 10^{-5}, 10^{-6}\}$. All models of the 2D network comparison train for a single strip with a batch size of 2.

To avoid non-invertible matrices $M = X^\top W X$ at the start of training, we pretrain Decomposer for 500 iterations, temporarily replacing the output transform with the field $T_\theta = \phi_\theta \odot \kappa_\theta$, where κ_θ are the voxel weights predicted by the network (Section 3.3.2), and \odot denotes voxel-wise multiplication. We initialize the rescaling weights of Encoder to 1 for translations and rotations, and to 0.05 for scaling and shear, which we find favorable to faster convergence.

Because SynthMorph training is generally not prone to overfitting, it uses a simple stopping criterion measuring progress P_i over batches $t \in S_i$ in terms of validation Dice overlap D (Section 4.3). The 3D models train with a batch size of 1 until the mean overlap across S_i exceeds $P_i = 99.9\%$ of the maximum, that is,

$$P_i = \left\{ |S_i| \max_{t \in S_i} D(t) \right\}^{-1} \sum_{t \in S_i} D(t). \quad (13)$$

For joint registration, we uniformly sample hyperparameter values $\lambda \in [0, 1]$. We freeze parameters θ of the trained affine submodel h_θ to fit only the weights ξ of hypernetwork Γ_ξ , optimizing the loss of Equation (5). While unfreezing the affine parameters θ within the setup of Figure 4 results in unchanged deformable accuracy, affine accuracy decreases. Although adding an affine loss term can prevent this decrease, we choose to train both stages separately—the third loss term increases complexity at no benefit, and simultaneous affine-deformable training requires more GPU memory.

4 Experiments

In a first experiment, we thoroughly analyze the performance of the different architectures across a broad range of variants and transformations, to understand how networks learn and best represent the affine component. In a second experiment, we select and train an architecture with synthetic data only. This experiment shifts the focus from network architectures to building a readily usable tool, and we assess the resulting accuracy in various affine registration tasks. In a third experiment, we complete the affine model with a deformable hypernetwork to produce a joint registration solution and compare its performance to readily usable baseline tools.

Table 1. Acquired test data for baseline comparisons spanning a range of MRI contrasts, resolutions, and subject populations. QIN includes contrast-enhanced clinical stacks of thick slices from patients with glioblastoma, whereas the other acquisitions use 3D sequences. While HCP-D and MASi include pediatric data, the remaining datasets consist of adult populations.

Dataset	Type	Voxel size (mm ³)	Pairs
UKBB	T1w, age 40–75 a	1.0×1.0×1.0	200
GSP	T1w, age 18–35 a	1.2×1.2×1.2	100
IXI	T1w	0.9×0.9×1.2	100
	T2w	0.9×0.9×1.2	100
	PDw	0.9×0.9×1.2	100
HCP-D	T1w, age 5–21 a	0.8×0.8×0.8	80
MASi	T1w, age 5–8 a	1.0×1.0×1.0	80
QIN	post-contrast T1w	0.4×0.4×6.0	50

4.1 Data

The training-data synthesis and analyses use 3D brain MRI from a very diverse collection of public data, aiming to truly capture the behavior of the methods facing the diversity of *real-world* images. While users of SynthMorph do not need to preprocess their data, our experiments use images conformed to the same isotropic $256 \times 256 \times 256$ 1-mm voxel space using trilinear interpolation, and by cropping and zero-padding symmetrically. We rearrange the voxel data to produce gross left-inferior-anterior (LIA) orientation with respect to the volume axes. Experiments conducted in 2D use corresponding mid-sagittal slices extracted from 3D images and label maps.

4.1.1 Generation label maps

For training-data synthesis, we compose a set of 100 whole-head tissue segmentations, each derived from T1w acquisitions with isotropic ~ 1 -mm resolution (although we do not use the T1w images in our experiments). The training segmentations include 30 locally scanned adult FSM subjects (Greve et al., 2021), 30 participants of the cross-sectional Open Access Series of Imaging Studies (OASIS, Marcus et al. 2007), 30 teenage subjects from the Adolescent Brain Cognitive Development study (ABCD, Casey et al. 2018), and 10 infants scanned at Boston Children’s Hospital at age 0-18 months (de Macedo Rodrigues et al., 2015; Hoopes et al., 2022b).

We derive brain label maps from the conformed T1w scans using SynthSeg (Billot et al., 2020). We emphasize that inaccuracies in the segmentations have little impact on our strategy, as the images synthesized from the segmentations will be in perfect voxel-wise registration with the labels by construction. To facilitate the synthesis of spatially complex image signals outside the brain, we use a simple thresholding procedure to add non-brain labels to each label map. The procedure sorts non-zero image voxels outside the brain into one of six intensity bins, equalizing bin sizes on a per-image basis.

4.1.2 Analysis and training images

For architecture analysis, we use T1w training images from 5000 adult participants of the UK Biobank (UKBB) study (Alfaro-Almagro et al., 2018; Miller et al., 2016; Sudlow et al., 2015). We also randomly pool 1000 distinct registration pairs from OASIS and another distinct 1000 pairs from ABCD to analyze real-world transforms.

4.1.3 Evaluation images

For baseline comparisons, we pool adult and pediatric T1w images from UKBB, the Brain Genomics Superstruct Project (GSP, Holmes et al. 2015), the Lifespan Human Connectome Project Development (HCP-D, Harms et al. 2018; Somerville et al. 2018), MASi-Var (MASi, Cai et al. 2021), and IXI (Imperial College London, 2015). The evaluation set also includes IXI scans with T2w and PDw contrast. As all these images are near-isotropic ~ 1 -mm acquisitions, we complement the dataset with contrast-enhanced clinical T1w stacks of axial 6-mm slices from subjects with newly diagnosed glioblastoma (QIN, Clark et al. 2013; Mamonov and Kalpathy-Cramer 2016; Prah et al. 2015).

Our experiments use the held-out test images listed in Table 1. For monitoring and model validation, we use a handful of images pooled from the same datasets, which do not overlap with the test subjects. We do not consider QIN at validation and validate performance in pediatric data with held-out ABCD subjects.

To measure registration accuracy, we compute anatomical brain label maps individually for each conformed image volume using SynthSeg (Billot et al., 2020). Although SynthMorph does not require skull-stripping, we skull-strip all images with SynthStrip (Hoopes et al., 2022b) for a fair comparison across images that have undergone the preprocessing steps expected by the baseline methods—unless explicitly noted.

4.1.4 Labels

The training segmentations encompass a set K of 38 different labels, 32 of which are standard (lateralized) FreeSurfer labels (Fischl et al., 2002). Parenthesizing their average size over FSM subjects relative to the total brain volume and combining the left and right hemispheres, these structures are: cerebral cortex (43.4%) and white matter (36.8%), cerebellar cortex (9.2%) and white matter (2.2%), brainstem (1.8%), lateral ventricle (1.7%), thalamus (1.2%), putamen (0.8%), ventral DC (0.6%), hippocampus (0.6%), caudate (0.6%), amygdala (0.3%), pallidum (0.3%), 4th ventricle (0.1%), accumbens (0.1%), inferior lateral ventricle (0.1%), 3rd ventricle (0.1%), and background.

The remaining labels map to variable image features outside the brain (Section 4.1.1). These added labels do not necessarily represent distinct or meaningful anatomical structures but expose the networks to non-brain im-

age content at training. We use all labels K to synthesize training images but optimize the overlap of brain-specific labels $J \subset K$ based on Equation (3).

For affine training and evaluation, we merge brain structures such that J consists of larger tissue classes: left and right cerebral cortex, left and right subcortex, and cerebellum. These classes ensure that small labels like the caudate do not have a disproportionate influence on global brain alignment—different groupings may work equally well. In contrast, deformable registration redefines J to include the 21 largest brain structures up to and including caudate. We use these labels for deformable training and evaluation, as prior analyses report that “only overlap scores of localized anatomical regions reliably distinguish reasonable from inaccurate registrations” (Rohlfing, 2011).

For a rigorous assessment of deformable registration accuracy, we separately consider the set of the 10 finest-grained structures above whose overlap we do *not* optimize at training, including the labels from amygdala through 3rd ventricle.

4.2 Baselines

We test affine and joint classical registration with ANTs (Avants et al., 2011) version 2.3.5 using recommended parameters (Pustina and Cook, 2017) for the NCC metric within and MI across MRI contrasts. We test NiftyReg (Modat et al., 2014) version 1.5.58 with the NMI metric and enable SVF integration for joint registration, as in our approach.

We also run the patch-similarity method Deeds (Heinrich et al., 2012), 2022-04-12 version. For a rigorous baseline assessment, we reduce the default grid spacing from $8 \times 7 \times 6 \times 5 \times 4$ to $6 \times 5 \times 4 \times 3 \times 2$. This setting effectively trades a shorter runtime for increased accuracy as recommended by the author, since it optimizes the parametric B-spline model on a finer control point grid (Heinrich et al., 2013). The modification results in a 1-2% accuracy improvement for most datasets as in prior work (Hoffmann et al., 2021a).

We test affine registration with `mri_robust_register` (“Robust”) from FreeSurfer 7.3 (Fischl, 2012) using its robust cost functions (Reuter et al., 2010), as only the robust cost functions can down-weight the contribution of regions that deform non-linearly. However, we highlight that the robust-entropy metric for cross-modal registration is experimental. We use Robust with up to 100 iterations and initialize the affine registration with a rigid run. Finally, we also test affine and deformable registration with the FSL (Jenkinson et al., 2012) tools FLIRT (Jenkinson and Smith, 2001) version 6.0 and FNIRT (Andersson et al., 2007) build 507. While the recommended cost function of FLIRT, correlation ratio, is suitable within and across modalities, we emphasize that users cannot change FNIRT’s MSE objective, which specifically targets within-contrast registration.

Table 2. Network capacity for model comparison. Each network uses a different width w held constant across its layers to reach a target capacity of 250k or 500k parameters, up to a small deviation.

Architecture	Config.	w	Capacity	Dev. (%)
Encoder	$C = 2^0$	72	252k	+0.8
Encoder	$C = 2^1$	45	250k	0.0
Encoder	$C = 2^2$	27	247k	+1.2
Encoder	$C = 2^3$	16	255k	+2.0
Encoder	$C = 2^4$	9	260k	+4.0
Decomposer	$n = 0$	63	253k	+1.2
Decomposer	$n = 1$	59	254k	+1.6
Decomposer	$n = 2$	55	248k	-0.8
Decomposer	$n = 3$	52	246k	-1.6
Detector	$k = 2^3$	62	248k	-0.8
Detector	$k = 2^4$	62	252k	+0.8
Detector	$k = 2^5$	61	253k	+1.2
Detector	$k = 2^6$	58	246k	-1.6
Encoder	$C = 2^0$	110	498k	-0.4
Decomposer	$n = 0$	89	504k	+0.8
Detector	$k = 2^5$	87	503k	+0.6

We compare DL model variants covering popular registration architectures in Section 4.4. This analysis uses the same capacity and training set for each model. For our final synthesis-based tool in Sections 4.5 and 4.6, we consider readily available machine-learning baselines trained by their respective authors, to assess their generalization capabilities to the diverse data we have gathered. This strategy evaluates what level of accuracy a user can expect from off-the-shelf methods without retraining, as retraining is generally challenging for users (see Section 5.4). We test: KeyMorph (Yu et al., 2022) and C2FViT (Mok and Chung, 2022) models trained for pair-wise affine, and the 10-cascade Volume Tweening Network (VTN) (Zhao et al., 2019b,d) trained for joint affine-deformable registration. Each network receives inputs with the expected image orientation, resolution, and intensity normalization.

4.3 Evaluation metrics

To measure registration accuracy, we propagate the moving label map s_m using the predicted transform T to obtain the moved label map $s_m \circ T$ and compute its (hard) Dice overlap D (Dice, 1945) with the fixed label map s_f . Since all baseline methods tested optimize an image-based objective, for a balanced comparison we also evaluate NCC of the modality-independent neighborhood descriptor (MIND, Heinrich et al. 2012) between the moved image $m \circ T$ and the fixed image f . As we seek to measure brain-specific registration accuracy, we remove any image content external to the brain labels prior to evaluating the image-based metrics. We use paired two-sided t -tests to determine whether differences in mean scores between methods are significant.

We analyze the regularity of deformation field ϕ in terms of the mean absolute value of the logarithm of the Jacobian determinant J_ϕ over spatial domain Ω . This quantity is sensitive to the deviation of J_ϕ from the ideal value 1 and thus provides a measure of the width of the distribution of log-Jacobian determinants, the “log-Jacobian spread” δ :

$$\delta(\phi) = \frac{1}{|\Omega^*|} \sum_{x \in \Omega^*} |\ln(|J_\phi(x)|)|, \quad (14)$$

where $\Omega^* = \{x \in \Omega \mid J_\phi(x) \neq 0\}$. We also determine the proportion of folding voxels, that is, locations $x \in \Omega$ where $J_\phi(x) < 0$. We compare the inverse consistency of registration methods by means of the average displacement E that voxels undergo upon subsequent application of transforms $\{T_1, T_2\}$,

$$E(T_1, T_2) = \frac{1}{|\Omega|} \sum_{x \in \Omega} \|(T_2 \circ T_1)(x) - x\|_2. \quad (15)$$

Specifically, we compute the inverse consistency of method h with $T_1 = h(m, f)$ and $T_2 = h(f, m)$ for any pair of input images $\{m, f\}$.

4.4 Experiment 1: network analysis

In the first experiment, we rigorously analyze variants and ablations of the three competing architectures from Section 3.3. Assuming a network capacity of $\sim 250k$ learnable parameters, our goal is to explore the relative strengths and weaknesses of the affine architectures, before we move on to training a network using the SynthMorph strategy.

4.4.1 Setup

The experiment compares networks in a 2D context, that is, at estimating 2D transforms with six degrees of freedom for pairs of image slices. A 2D setup for learning unsupervised registration by minimizing an NCC loss enables us to reduce the computational burden and thus explore numerous model configurations. We train networks drawing $\{m, f\}$ from a set of 5000 T1w UKBB images, and test registration on a validation set of 100 cross-subject pairs that does not overlap with the training data. To keep network capacities similar, each model has a different width w , held constant across its convolutional layers as shown in Table 2. Training uses only affine augmentation as indicated in Table B.1.

First, we assess to what extent Encoder benefits from weight sharing. We train models with different numbers $C \in \{1, 2, 4, 8, 16\}$ of subnetworks that either share or use separate weights.

Second, we compare Decomposer variants that fit T in an OLS sense, using weights $\forall x \in \Omega, \kappa_\theta(x) = 1$, or in a WLS sense. For both, we assess how increasing the resolution ρ of the field ϕ_θ relative to f affects performance, by upsampling by a factor of 2 after each of the

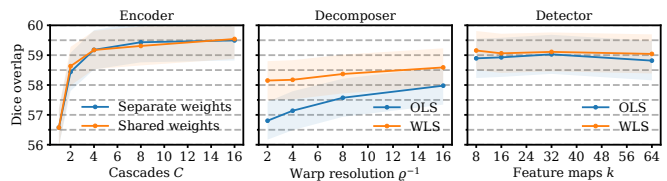


Figure 6. Network analysis. We assess Encoder with different numbers of subnetworks C . We also analyze Decomposer and Detector variants using ordinary (OLS) or weighted least squares (WLS), exploring the effect of varying the warp resolution ρ relative to the input image size and different numbers of output feature maps k , respectively. Dice scores are averages over 100 UKBB cross-subject 2D pairs. Shaded areas indicate the standard error of the mean.

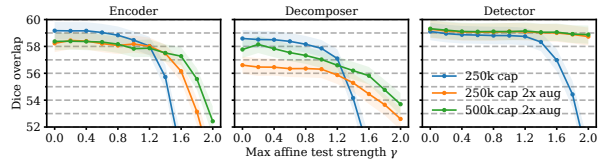


Figure 7. Network robustness across affine transform strengths γ relative to the augmentation range of Table B.1. At a given γ , we resample each image of the validation set with affine parameters drawn from a uniform distribution \mathcal{U} modulated by γ , for example rotation angle $r \sim \mathcal{U}(-\gamma\alpha, \gamma\alpha)$, where $\alpha = 45^\circ$. We also test networks trained with doubled augmentation (aug) and doubled capacity (cap). Dice scores are averages over 100 UKBB cross-subject 2D pairs. Shaded areas indicate the standard error of the mean.

first $n \in \{0, 1, 2, 3\}$ convolutional blocks following the encoder, using skip connections where possible, such that $\rho(n) = 1/2^{4-n}$.

Third, we analyze OLS and WLS variants of Detector predicting $k \in \{8, 16, 32, 64\}$ feature maps to compute the corresponding (a_i, p_i) and (b_i, q_i) for $i \in \{1, 2, \dots, k\}$.

Finally, we select a suitable configuration per architecture and analyze its performance across a range of transformation magnitudes. We investigate how models adapt to larger transforms, by fine-tuning pretrained weights to twice the affine augmentation amplitudes of Table B.1 until convergence, and we also repeat the experiment with doubled capacity. We test on copies of the UKBB validation set, each injected with random affine transforms of maximum strength $\gamma \in [0, 2]$ relative to the augmentation range of Table B.1. For example, at a given γ , we uniformly sample a rotation angle $r \sim \mathcal{U}(-\gamma\alpha, \gamma\alpha)$ for each of the 200 moving and each fixed images, where $\alpha = 45^\circ$, and similarly for all other degrees of freedom (DOF), that we apply by resampling the image (Appendix A).

4.4.2 Results

Figure 6 compares registration accuracy for the NCC-trained model configurations in terms of Dice overlap. Encoder achieves the highest accuracy, surpassing the best Detector configuration by up to 0.4 and the best Decomposer by up to 1 Dice point. Using more subnetworks improves Encoder performance, albeit with diminishing returns after $C = 4$ and at the cost of substantially

longer training times that roughly scale with C .

The local rescaling weights of subnetwork h_1 converge to values around 1 for translations and rotations and around 0.01 for scaling and shear. The values tend to decrease for subsequent h_i ($i > 1$), most noticeably the translational weights. For h_C , the translational weights converge to roughly 50% of those of h_1 , suggesting that

the first subnetworks perform the bulk of the alignment, whereas the subsequent h_i refine it by smaller amounts.

Although keeping subnetwork weights separate might also enable each h_i to specialize in increasingly fine adjustments to the final transform, in practice we observe no benefit in distributing capacity over the subnetworks compared to weight sharing. Decomposer shows a clear trend towards lower output resolutions ϱ improving accuracy. While decomposing the field ϕ_θ in a WLS sense boosts performance by 0.6–1.3 points over OLS, the model still lags behind the other architectures while requiring 2–3 times more training iterations to converge. There is little difference across numbers k of output feature maps, and choosing WLS over OLS slightly increases in accuracy.

Figure 7 shows network robustness across a range of maximum transform strengths γ , where we compare Encoder with $C = 4$ subnetworks sharing weights to the WLS variants of Decomposer without upsampling and Detector with $k = 32$ output channels, to balance performance and efficiency.

Detector proves most robust to large transforms, remaining unaffected up to $\gamma \approx 1.2$, i.e. shifts and rotations up to 36 mm and 54° for each axis, respectively, and scale and shear up to 0.12. In contrast, accuracy declines substantially for Encoder and Decomposer after $\gamma \approx 0.8$, corresponding to maximum transforms of 24 mm and 36° (blue). Doubling the affine augmentation extends Encoder and Decomposer robustness to $\gamma \approx 1.2$ but comes at the cost of a drop of 1 and 2 Dice points for all $\gamma < 1.2$, respectively (orange). Decomposer performance is capacity-bound, as doubling the number of parameters restores $\sim 50\%$ of the drop in accuracy, whereas increasing capacity does not improve Encoder accuracy for $\gamma < 1.2$ (green). Detector optimally benefits from the doubled affine augmentation, which enables the network to perform robustly across the test range (orange). Doubling capacity has no effect (green).

In conclusion, the marginal lead of Encoder only manifests for small transforms and at $C = 16$ cascades. The 16 interpolation steps of this variant render it intractably inefficient for 3D applications. In contrast, Detector performs with high accuracy across transformation strengths, making it a more suitable architecture for a general registration tool.

4.5 Experiment 2: affine tool performance

Based on the accurate performance of Detector and its robustness across transform strengths shown in Section 4.4 in 2D and prior work (Yu et al., 2022) in 3D, we train the WLS-based architecture in 3D using the generative strategy of Figure 2, leading to “affine SynthMorph”. We focus on the development of an anatomy-aware affine registration tool that generalizes across MRI acquisition protocols while enabling brain registration without requiring the user to preprocess data.

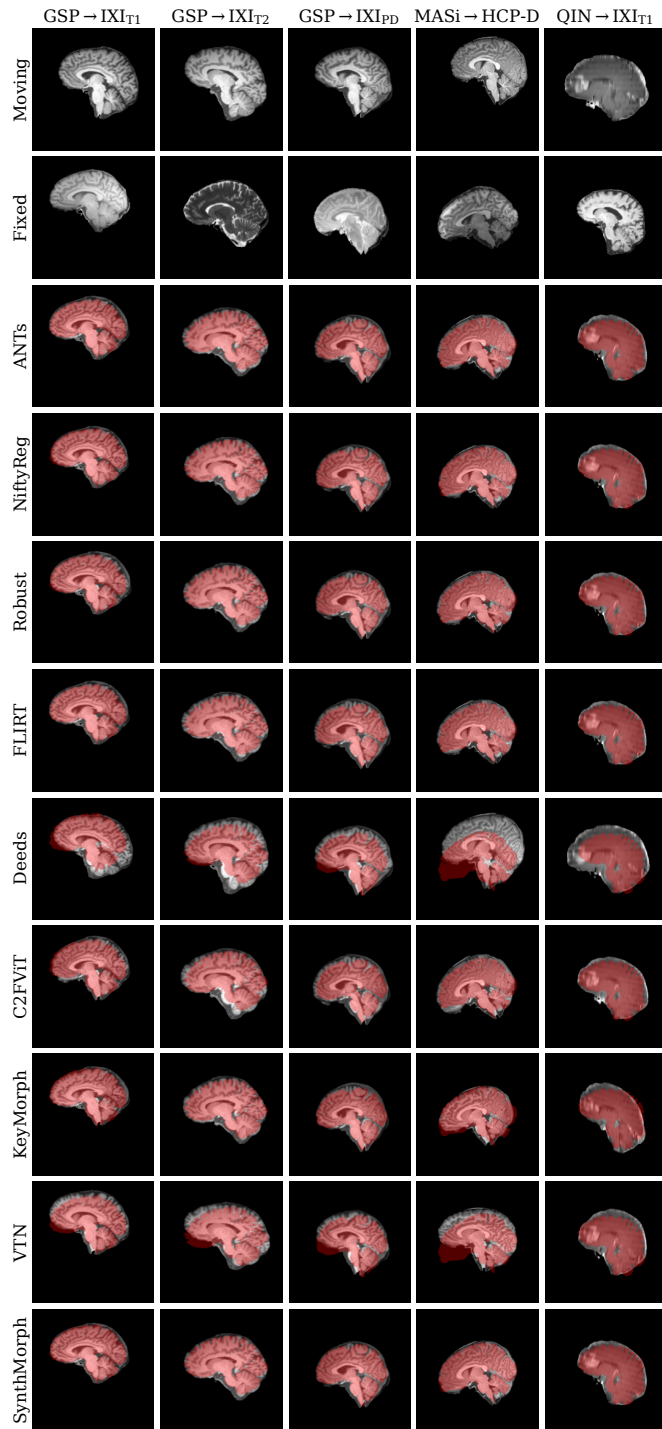


Figure 8. Representative affine 3D registration examples showing the image moved by each method overlaid with the fixed brain mask (red). Each row is an example from a different dataset.

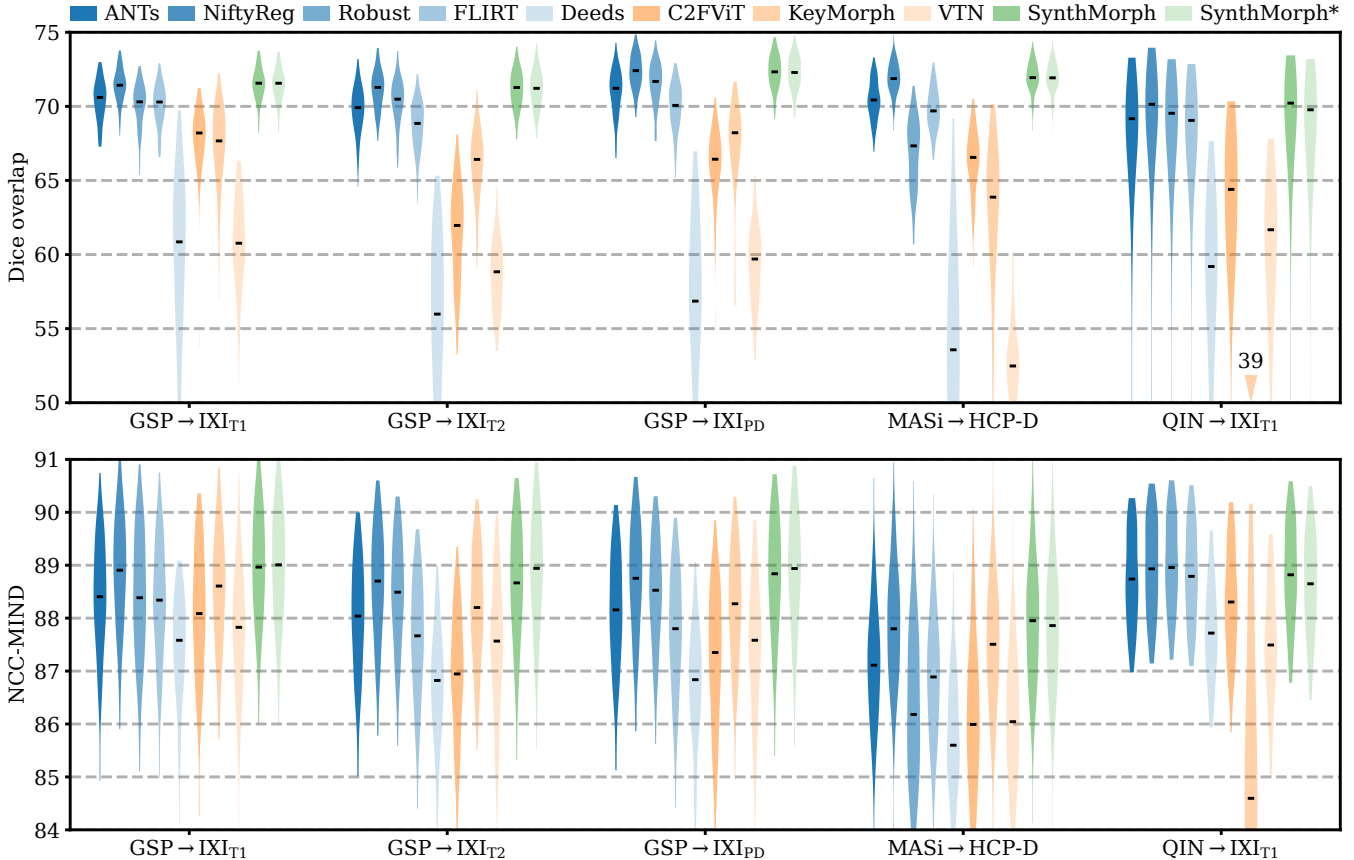


Figure 9. Affine 3D registration accuracy as mean Dice scores and in terms of image similarity. Each violin shows the distribution across the skull-stripped cross-subject pairs from Table 1. For comparison, the asterisk indicates SynthMorph performance without skull-stripping. Downward arrows indicate median scores outside the plotted range. Metric values range from 0 to 100. Higher is better.

4.5.1 Setup

First, to give the reader an idea of the accuracy achievable with off-the-shelf algorithms for data unseen at training, we compare affine SynthMorph to classical and DL baselines trained by the respective authors. We test affine registration of skull-stripped images across MRI contrasts, for a variety of different imaging resolutions and populations, including adults, children, and patients with glioblastoma. We also compare the symmetry of each method with regard to reversing the order of input images. Each test involves held-out image pairs from separate subjects, summarized in Table 1.

Affine SynthMorph implements Detector (Figure 5) with $w = 256$ convolutional filters, as this network width proved adequate for learning registration from synthetic data (Hoffmann et al., 2021a). Using 3D convolutions, we choose $k = 64$ output feature maps, shown to yield best performance for large 3D transforms (Yu et al., 2022). We train SynthMorph solely with synthetic images generated from label maps using the hyperparameters of Table B.1.

Second, we analyze the effect of thick-slice acquisitions on affine SynthMorph accuracy compared to classical baselines. This experiment retrospectively reduces

the through-plane resolution of the moving image of each $\text{GSP} \rightarrow \text{IXI}_{T1}$ pair to produce stacks of axial slices of thickness $\Delta z \in \{1, 2, \dots, 10\}$ mm. At each Δz , we simulate partial voluming (Kneeland et al., 1986; Simmons et al., 1994) by smoothing all moving images in slice-normal direction with a 1D Gaussian kernel of full-width at half-maximum (FWHM) Δz and by extracting slices Δz apart using linear interpolation. Finally, we restore the initial volume size by linearly upsampling the through-plane.

Third, we evaluate the importance of skull-stripping the input images for accurate registration. With the exception of skull-stripping, we preprocess full-head $\text{GSP} \rightarrow \text{IXI}_{T1}$ pairs as expected by each method and assess brain-specific registration accuracy by evaluating image-based metrics within the brain only.

4.5.2 Results

Figure 8 shows representative registration examples for the tested dataset combinations, while Figure 9 quantitatively compares affine registration accuracy across skull-stripped image pairings. Although affine SynthMorph has not seen any real MRI data at training, it achieves the highest Dice score for every dataset tested.

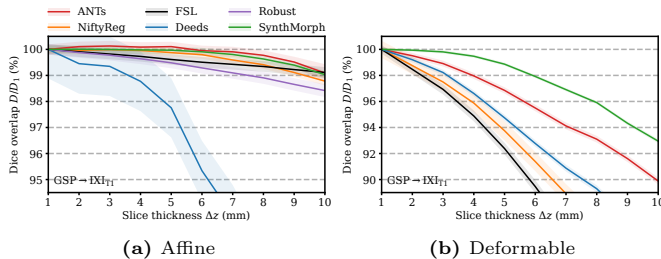


Figure 10. Dependency of 3D (a) affine and (b) deformable registration accuracy on slice thickness. For comparability, we initialize all deformable tools with affine transforms estimated by NiftyReg. Each value indicates the mean over 100 skull-stripped pairs (higher is better). Shaded areas indicate the standard error of the mean.

Table 3. Single-threaded runtimes on a 2.2-GHz Intel Xeon Silver 4114 CPU, averaged over $n = 10$ runs. Errors indicate standard deviations. On an NVIDIA V100 GPU, all affine and deformable DL runtimes (below midline) are about 1 minute, including setup.

Method	Affine (sec)	Deformable (sec)
ANTs	777.8 ± 36.0	17189.5 ± 52.7
NiftyReg	293.7 ± 0.5	7021.0 ± 21.3
Deeds	142.8 ± 0.3	383.1 ± 0.6
Robust	1598.9 ± 0.8	–
FSL	151.7 ± 0.4	8141.5 ± 195.7
C2FViT ¹	43.7 ± 0.3	–
KeyMorph	36.2 ± 2.6	–
VTN ²	–	63.5 ± 0.3
SynthMorph	72.4 ± 0.8	887.4 ± 2.5

¹ Timed on the GPU as the device is hard-coded.

² Implementation performs joint registration only.

For the GSP→IXI_{T1} and MASi→HCP-D pairs that most baselines are optimized for, SynthMorph exceeds the best-performing baseline NiftyReg by $\Delta D = 0.1$ points ($p < 10^{-4}$ and $p < 0.03$ for paired two-sided t -tests). Across all other pairings, SynthMorph matches the Dice score achieved by the most accurate affine baseline, which is NiftyReg in every case.

Deeds performs least accurately, lagging behind the second last classical baselines by $\Delta D = 10.1$ or more. The other classical methods perform robustly across all testsets, generally within 1–2 Dice points of each other.

On the MASi→HCP-D testset, FLIRT’s performance exceeds Robust by $\Delta D = 3$ ($p = 10^{-23}$) and matches it across GSP→IXI_{T1} pairs ($p = 0.8$). Across the remaining testsets, FLIRT ranks fourth among classical baselines.

In contrast, the DL baselines do not reach the same accuracy. Even for the T1w pairs they were trained with, SynthMorph leads by $\Delta D = 3.7$ or more, likely due to domain shift between the test and baseline training data. As expected, DL-baseline performance continues to decrease as the test-image characteristics deviate further from those at training. Interestingly, VTN consistently ranks among the least accurate baselines, although its preprocessing effectively initializes the translation and scaling parameters by separately adjusting the moving

and fixed images such that the brain fills the whole FOV.

Even though affine SynthMorph does not directly optimize image similarity at training, it surpasses NiftyReg for GSP→IXI_{T1} ($p < 2 \times 10^{-11}$) and MASi→HCP-D ($p < 0.02$) pairs in terms of the image-based NCC-MIND metric. Generally, NCC-MIND ranks the methods similarly to Dice overlap, as does NCC (not shown) across the T1w registration pairs.

Figure 11 shows that SynthMorph’s affine symmetry outperforms all baselines tested across GSP→IXI_{T1} pairs. When we reverse the order of the input images, the inconsistency between forward and backward transforms is $E = 0.003\%$ of the voxel size, tightly followed by NiftyReg. Robust also uses an inverse-consistent algorithm, leading to $E = 0.4\%$. The remaining baselines are substantially less symmetric, with inconsistencies of $E = 100\%$ of the voxel size for KeyMorph or more.

Figure 10a shows how registration accuracy evolves with increasing moving-image slice thickness Δz . SynthMorph and ANTs remain the most robust for $\Delta z \leq 6$ mm, reducing to 99% at $\Delta z = 10$ mm. For $\Delta z \in [2, 5]$ mm, ANTs accuracy even improves slightly, likely benefiting from the smoothing effect on the images. The classical baselines FLIRT and Robust are only mildly affected by thicker slices. While their Dice scores decrease more rapidly for $\Delta z \leq 8$, their accuracy reduces to 99% and about 98.5% at $\Delta z = 10$ mm. Deeds is noticeably more susceptible to resolution changes, decreasing to less than 95% at $\Delta z > 6.5$ mm.

Figure 12 compares the drop in median Dice overlap the affine methods undergo for full-head as opposed to skull-stripped GSP→IXI_{T1} images. Except for Deeds, brain-specific accuracy reduces substantially, by 3% in the case of NiftyReg and up to 8% for ANTs. Affine SynthMorph remains most robust: its Dice overlap changes by less than 0.05%. Deeds is the only method that sees accuracy increase but still yields the lowest score for the testset.

Table 3 lists the registration time required by each affine method on a 2.2-GHz Intel Xeon Silver 4114 CPU using a single computational thread. The values shown reflect averages over $n = 10$ uni-modal runs. Classical runtimes range between 2 and 27 minutes with Deeds being the fastest and Robust being the slowest, although we highlight that we substantially increased the number of Robust iterations. Complete single-threaded DL runtimes are about 1 minute, including model setup. However, inference only takes a few seconds and reduces to well under a second on an NVIDIA V100 GPU.

4.6 Experiment 3: joint registration

Motivated by the affine performance of SynthMorph, we complete the model with a hypernetwork-powered deformable module to achieve 3D joint affine-deformable registration (Figure 4). Our focus is on building a complete and readily usable tool that generalizes across scan protocols while requiring minimal preprocessing.

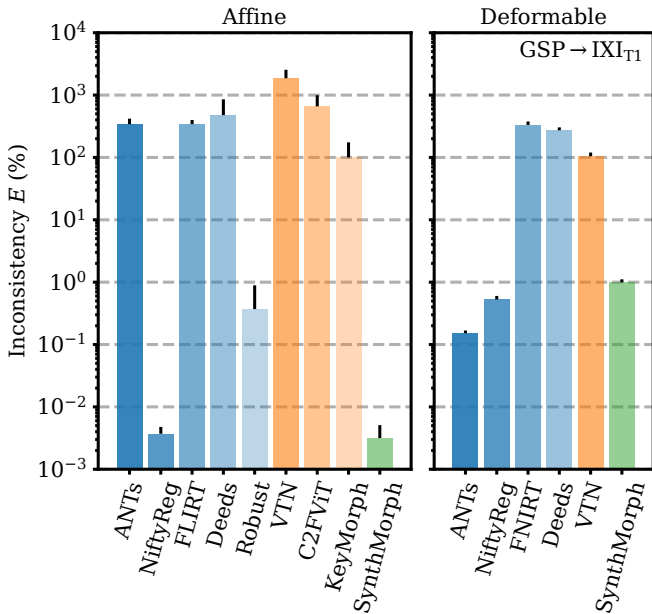


Figure 11. Forward-backward inconsistency between transforms when reversing the order of input images. We compare the mean displacement of voxels upon subsequent application of both transforms, relative to the voxel size. Lower values are better.

4.6.1 Setup

First, we compare deformable registration using the held-out image pairs from separate subjects for each of the datasets of Table 1. The comparison employs skull-stripped images initialized with affine transforms estimated by NiftyReg, the most accurate baseline in Figure 9. We compare deformable SynthMorph performance to classical baselines and VTN, the only joint DL baseline trained by the original authors that is available to us—we seek to gauge the accuracy achievable with off-the-shelf algorithms for data unseen at training.

Second, we analyze robustness to sub-optimal affine initialization. In order to cover realistic affine inaccuracies and assess the most likely and intended use case, we repeat the previous experiment, this time initializing each method with the affine transform obtained with the same method—that is, we test end-to-end joint registration with each tool. Similarly, we evaluate the importance of removing non-brain voxels from the input images. In this experiment, we initialize each method with affine transforms estimated by NiftyReg from skull-stripped data, and test deformable registration of full-head images.

Third, we analyze the effect of reducing through-plane resolution Δz on SynthMorph performance compared to classical baselines, following the steps outlined in Section 4.5. In this experiment, we initialize each method with affine transforms estimated by NiftyReg from skull-stripped images, such that the comparison solely reflects deformable registration accuracy.

Fourth, we analyze warp-field regularity and registration accuracy over dataset $GSP \rightarrow IXI_{T1}$ as a function of

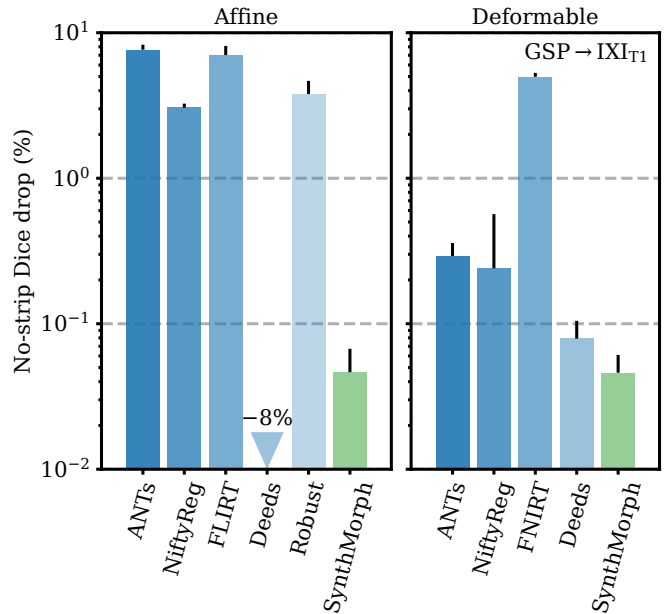


Figure 12. Relative reduction in brain-specific accuracy when registering full-head instead of skull-stripped images. Lower values are better. Although affine Deeds is the only method whose Dice overlap increases, it still ranks as the least accurate on the $GSP \rightarrow IXI_{T1}$ testset. Error bars show the standard error of the mean.

the regularization weight λ . We also compare the symmetry of each method with regard to reversing the order of the input images.

4.6.2 Results

Figure 13 shows typical deformable registration examples for each method, and Figure 14 quantitatively compares registration accuracy across testsets in terms of mean Dice overlap D over the 21 largest anatomical structures (large-21), 10 fine-grained structures (small-10) not optimized at training, and image similarity measured with NCC-MIND. Supplemental Figures S.1–S.5 show deformable registration accuracy across individual brain structures.

Although SynthMorph trains with synthetic images only, it achieves the highest large-21 score for every skull-stripped testset. For all cross-contrast pairings and the pediatric testset, SynthMorph leads by at least 1.7 Dice points compared to the highest baseline score ($MASi \rightarrow HCP-D$, $p < 10^{-22}$ for paired two-sided t -test) and often much more. Across these testsets, SynthMorph performance remains largely invariant, whereas the other methods except Deeds struggle. Crucially, the distribution of SynthMorph scores for isotropic data is substantially narrower than the baseline scores, indicating the absence of gross inaccuracies such as pairs with $D < 65$ that several baselines yield across all isotropic contrast pairings. On the clinical testset $QIN \rightarrow IXI_{T1}$, SynthMorph surpasses the baselines by at least $\Delta D = 5.1$. For $GSP \rightarrow IXI_{T1}$, it outperforms the best classical baseline ANTs by 1 Dice point ($p < 10^{-18}$).

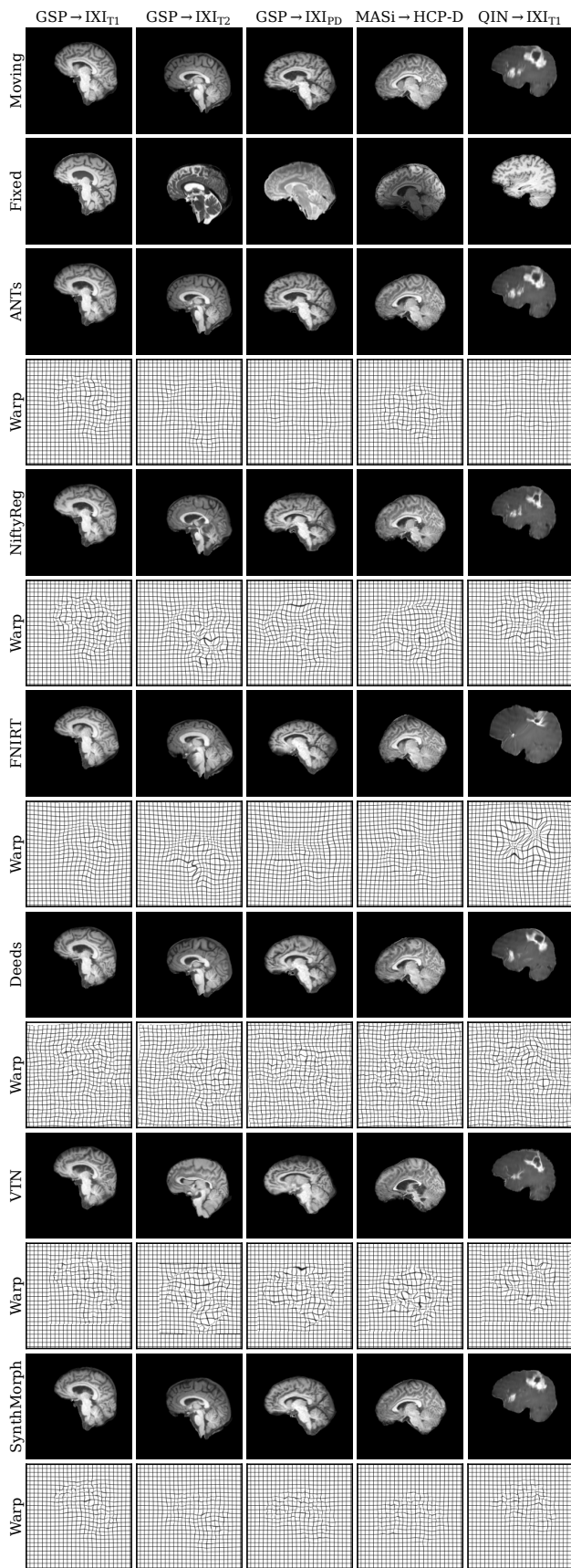


Figure 13. Deformable 3D registration examples comparing the moved image $m \circ \phi$ and the deformation field ϕ across methods. Each row is an example from a different dataset. For comparability, we initialize all methods with NiftyReg’s affine registration.

Across the T1w testsets, FNIRT outperforms NiftyReg by several Dice points and also ANTs for MASi→HCP-D pairs. Surprisingly, FNIRT beats NiftyReg’s NMI implementation for GSP→IXI_{T2}, even though FNIRT’s cost function targets within-contrast registration. The most robust baseline is Deeds, which ranks third at adult T1w registration. Its performance reduces the least for the cross-contrast and clinical testsets, where it achieves the highest Dice overlap after SynthMorph.

The only joint DL baseline with trained weights that we had access to, VTN, yields relatively low accuracy across all testsets. This was expected for the cross-contrast pairings, since the model was trained with T1w data, confirming the data dependency introduced with standard training. However, VTN lags behind the worst-performing classical baseline for GSP→IXI_{T1} data, NiftyReg, too ($\Delta D = 2.1$, $p < 3 \times 10^{-7}$), likely due to domain shift as in the affine case.

Considering the fine-grained small-10 brain structures held out at training, SynthMorph consistently ranks among the two best-performing methods, matching the performance of Deeds for GSP→IXI_{T1} ($\Delta D = 0.1$, $p = 0.7$) and GSP→IXI_{PD} ($\Delta D = 0.2$, $p = 0.3$), and leading by at least $\Delta D > 5$ ($p < 3 \times 10^{-10}$) on the clinical testset.

Interestingly, SynthMorph outperforms all baselines across testsets in terms of NCC-MIND ($p < 2 \times 10^{-17}$), although it is the only method not optimizing or trained with an image-based loss.

Figure 15 shows the relative change in large-21 Dice for each tool when run end-to-end compared to affine initialization with NiftyReg. SynthMorph’s drop in performance is 0.05% or less across all datasets. For GSP→IXI_{T1}, classical-baseline accuracy decreases by no more than 0.3%. Across the other datasets, the classical methods generally cannot make up for the discrepancy between their own and NiftyReg’s affine transform: accuracy drops by up to 4.9%, whereas SynthMorph remains robust. The performance of VTN reduces by at least 7.3% across testsets and often much more, highlighting the detrimental effect an inaccurate affine transform can have on the subsequent deformable step. Figure 12 shows the importance of skull-stripping for deformable registration accuracy. Generally, deformable accuracy suffers less than affine registration when switching to full-head images, as these algorithms can deform different image regions independently. SynthMorph remains most robust to the change in preprocessing; its large-21 Dice overlap reduces by less than 0.05%. With a drop of 0.08%, Deeds is similarly robust. In contrast, FNIRT’s performance is most affected and reduces by 5%—a decline of the same order as for most affine methods.

Figure 16 analyzes SynthMorph warp smoothness. As expected, image-based NCC-MIND and large-21 Dice accuracy peak for weak regularization of $\lambda < 0.2$. In contrast, overlap of the small-10 regions not optimized at training benefits from smoother warps, with an optimum at $\lambda = 0.4$. The fields predicted by SynthMorph achieve

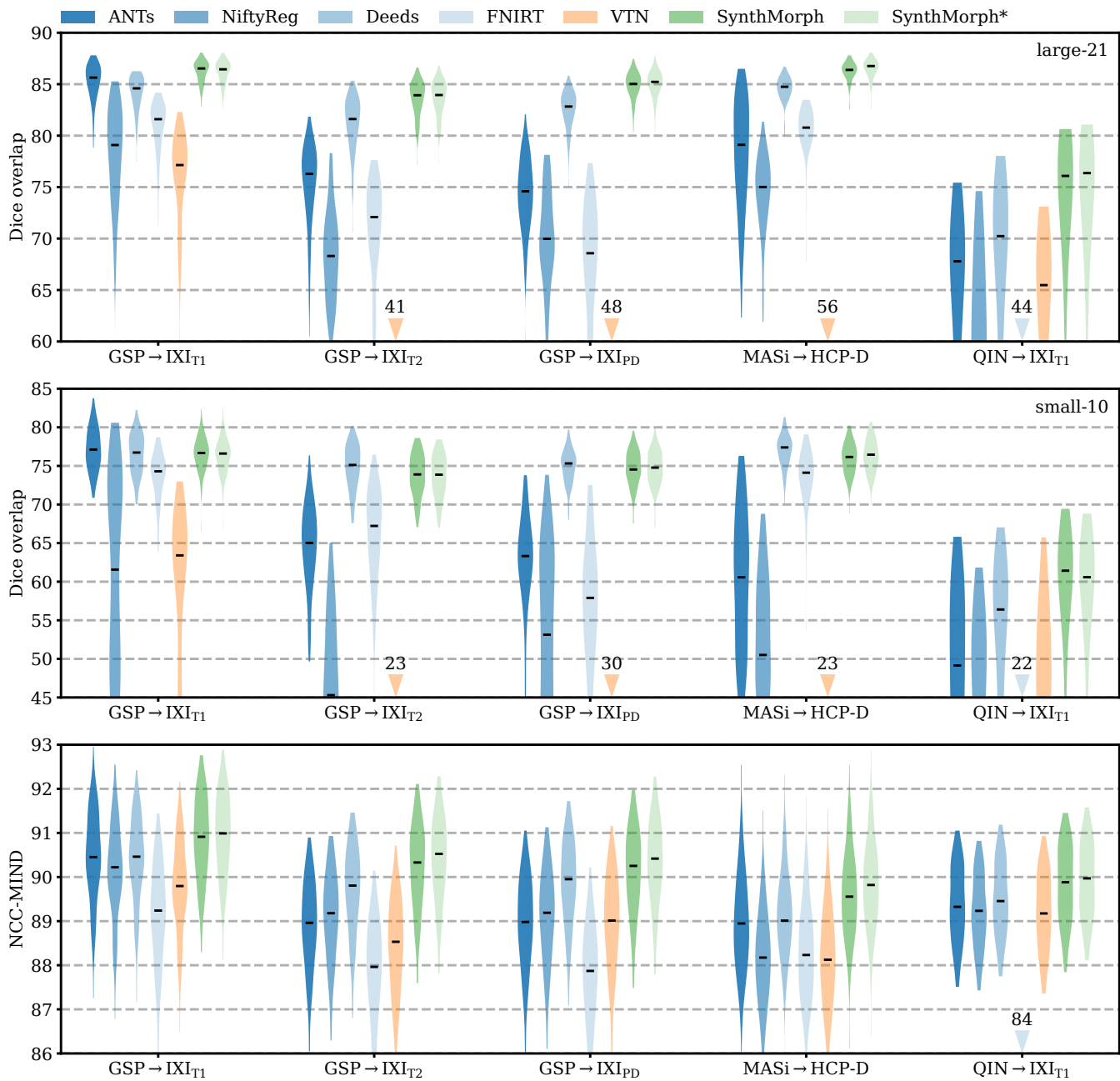


Figure 14. Deformable 3D registration accuracy as mean Dice scores over the 21 largest brain regions (large-21), 10 fine-grained structures not optimized at SynthMorph training (small-10), and image similarity. Each violin shows the distribution across the skull-stripped cross-subject pairs from Table 1. For comparability, we initialize all deformable tools with affine transforms estimated by NiftyReg. The asterisk indicates SynthMorph performance without skull-stripping. Downward arrows show median scores outside the plotted range. Higher values are better.

the lowest log-Jacobian spread across all baselines for $\lambda > 0.4$ and are thus closest to the ideal value 1. Similarly, the proportion of folding voxels decreases with higher λ and drops to 0% at $\lambda = 0.5$ (10 integration steps). Deeds is the weakest-regularized method and yields $6 \times 10^{-5}\%$ folding voxels, whereas the other baselines achieve 0%. For realistic warp fields with characteristics that match or exceed the tested baselines, we conduct all comparisons in this study with a default weight $\lambda = 0.5$. We highlight that λ is an input to SynthMorph, enabling users to

choose the optimal regularization strength for their specific data without retraining.

Deformable registration with SynthMorph is highly symmetric (Figure 11), with a forward-backward inconsistency of only 1% of the voxel size, that closely follows ANTs (0.2%) and NiftyReg (0.5%). In contrast, the other methods have inconsistencies of the order of the voxel size.

Figure 10b assesses the dependency of registration performance on slice thickness Δz . Similar to the affine case, deformable accuracy decreases for thicker slices, albeit

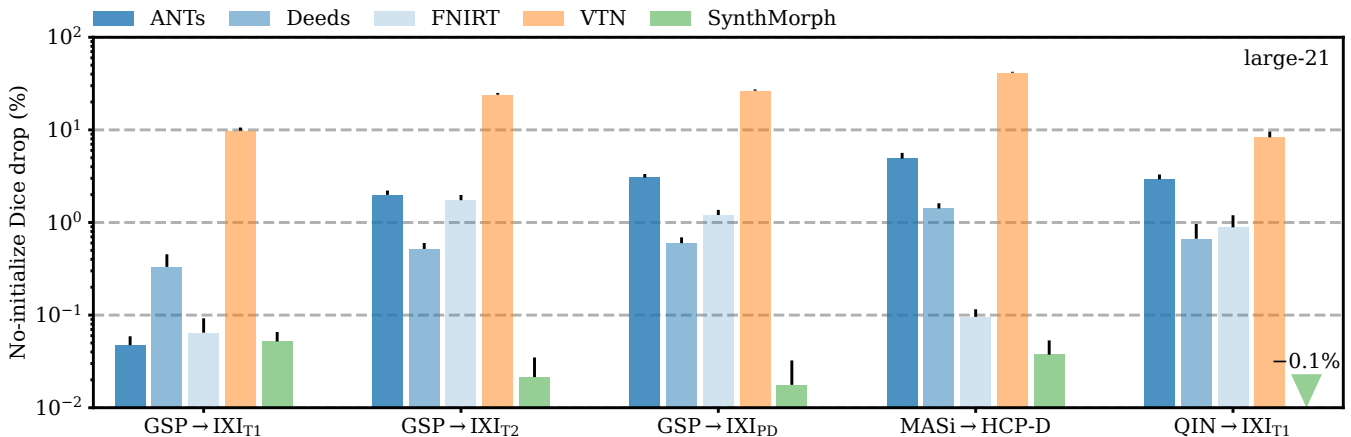


Figure 15. Mean decrease in Dice scores for end-to-end joint registration relative to affine initialization with NiftyReg. Except for adult T1w registration pairs, the classical tools in blue generally cannot compensate for the discrepancy between their own and NiftyReg’s affine transform, showing the devastating effect inaccurate affine initialization can have on subsequent deformable registration.

faster. SynthMorph performs most robustly. Its accuracy remains unchanged up to $\Delta z \leq 3$ mm and reduces 95% at $\Delta z = 8.5$ mm. ANTs is the most robust classical method, but its accuracy drops considerably faster than SynthMorph. FLIRT and NiftyReg are most affected at reduced resolution, performing at less than 95% accuracy for $\Delta z \geq 4$ mm and $\Delta z \geq 4.5$, respectively.

Deformable registration often requires substantially more time than affine registration (Table 3). On the GPU, SynthMorph takes less than 8 seconds per image pair for registration, IO, and resampling. One-time model setup requires about 1 minute, after which the user could register any number of image pairs without reinitializing the model. On the CPU, the fastest classical method Deeds requires only about 6 minutes in single-threaded mode, whereas ANTs takes almost 5 hours. While VTN’s joint runtime is 1 minute, SynthMorph needs about 15 minutes for deformable registration on a single thread.

5 Discussion

We present an easy-to-use DL tool for end-to-end affine and deformable brain registration. SynthMorph achieves robust performance across imaging contrast, resolution, and pathology, enabling accurate registration for brain scans right off the scanner without preprocessing. The SynthMorph strategy alleviates the dependency on acquired training data by generating widely variable images from anatomical label maps—and there is no need for label maps at registration time.

5.1 Architectures

We performed a rigorous analysis of popular affine architectures. The comparison shows that Encoder is an excellent network architecture if the expected transforms are small, especially at a number of cascades $C \geq 4$. For medium to large transforms, Encoder accuracy suffers.

While our experiments indicate that the reduction in accuracy can be mitigated by simultaneously optimizing a separate loss for each cascade, doing so substantially increases training times compared to the other architectures. Another drawback of Encoder is the image-size dependence introduced by the FC layer. We find that Detector is a more flexible and robust alternative for medium to large transforms. A limitation of the 2D network analysis is that the results may not generalize fully to 3D registration. The comparison only serves as an indication of the relative strengths and weaknesses of the architectures. Yet, prior work confirms the robustness of Detector across large transforms in 3D (Yu et al., 2022).

Vision transformers (Dosovitskiy et al., 2020) are another popular approach to overcoming the local receptive field of convolutions with small kernel sizes, querying information across distributed image patches. However, in practice the sophisticated architecture is often unnecessary for many computer-vision tasks (Pinto et al., 2022); while simple small-kernel U-Nets generally perform well as their multi-resolution convolutions effectively widen the receptive field (Liu et al., 2022b), increasing the kernel size can boost the performance of convolutional networks beyond that achieved by vision transformers across multiple tasks (Ding et al., 2022; Liu et al., 2022a).

5.2 Anatomy-specific registration

Accurate registration of the specific anatomy of interest requires down-weighting the contribution of irrelevant image content to the optimization metric. SynthMorph *learns* what anatomy is pertinent to the task, as we optimize the overlap of select labels of interest only. It is likely that the model learns an implicit segmentation of the image, in the sense that it focuses on deforming the anatomy of interest, warping the remainder of the image only to satisfy regularization constraints. In contrast, most classical and DL methods cannot distinguish between rele-

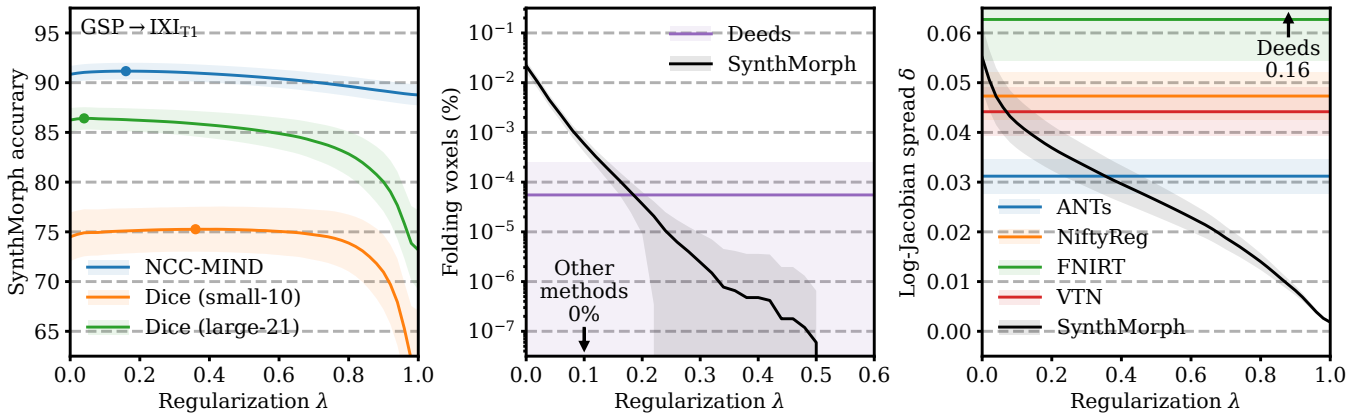


Figure 16. Regularization analysis of SynthMorph registration accuracy, the proportion of folding voxels with a negative Jacobian determinant, and the spread of the distribution of absolute log-Jacobian determinants as a function of the regularization weight λ . The dots indicate maximum accuracy. For the other metrics, lower values are better.

vant and irrelevant image features, and thus have to rely on explicit segmentation to remove distracting content prior to registration, such as skull-stripping in neuroimage processing (Eskildsen et al., 2012; Hoopes et al., 2022b; Iglesias et al., 2011; Salehi et al., 2017; Smith, 2002).

SynthMorph does not enforce or assume a hard segmentation: while our implementation starts with discrete labels, the input could, in principle, be a set of probability maps indicating the likelihood that each image region belongs to a particular tissue class. In fact, the interpolation of the one-hot encoded label maps during training already introduces soft edges that vary smoothly from 0 outside to 1 inside each structure.

Pathology missing from the training labels does not necessarily hamper overall registration accuracy, as the experiments with scans from patients with glioblastoma show. In fact, SynthMorph outperforms all deformable baselines tested on these data. However, we do not expect these missing structures to be mapped with high accuracy, in particular if the structure is absent in one of the test images—this is no different from the behavior of methods optimizing image similarity. In this work, we train SynthMorph as a general tool for cross-subject registration. For specialized applications such as tumor tracking, performance may be limited relative to a dedicated model. Pathology-specific models could be trained by extending our strategy, adding synthesized pathology labels to segmentation maps from healthy subjects.

5.3 Baseline performance

Networks trained with the SynthMorph strategy do not have access to the MRI contrasts of the testsets nor in fact to any MRI data at all. Yet SynthMorph matches or outperforms classical and DL-baseline performance across the real-world datasets tested, while being substantially faster than the classical methods. For deformable registration, the fastest classical method Deeds requires 6 minutes, while SynthMorph takes about 1 minute for one-

time model setup and just under 8 seconds for each subsequent registration. This speed-up may be particularly useful for processing large datasets like ABCD, enabling end-to-end registration of hundreds of image pairs per hour—the time that some established tools like ANTs require for a single registration.

The DL baselines tested have runtimes comparable to SynthMorph. Combining them with skull-stripping would generally be a viable option for fast brain-specific registration: brain extraction with a tool like SynthStrip only takes about 30 seconds. However, we are not aware of any existing DL tool that would enable deformable registration of unseen data with adjustable regularization strength *without* retraining. While the DL baselines break down for contrasts unobserved at training, they also cannot match the accuracy of classical tools for the T1w contrast they were trained on, likely due to domain shift.

In contrast, SynthMorph performance is relatively unaffected by changes in imaging contrast, resolution, or subject population. These results demonstrate that the SynthMorph strategy produces powerful networks that can register new image types unseen at training. We emphasize that our focus is on leveraging the training strategy to build a robust and accurate registration tool. It is possible that other architectures, such as the trained DL baselines tested in this work, perform equally well when trained using our strategy.

Although Robust down-weights the contribution of image regions that cannot be mapped with the linear transformation model of choice, its accuracy dropped by several points for data without skull-stripping. The poor performance in cross-contrast registration may be due to the experimental nature of its robust-entropy cost function. We initially experimented with the recommended NMI metric, but registration failed for a number of cases as Robust produced non-invertible matrix transforms, and we hoped that the robust metrics would deliver accurate results in the presence of non-brain image content—which the NMI metric cannot ignore during optimization.

5.4 Challenges with retraining baselines

Retraining DL baselines to improve performance for specific user data involves substantial practical challenges. For example, users have to reimplement the architecture and training setup from scratch if code is not available. If code is available, the user may be unfamiliar with the specific programming language or machine-learning library, and building on the original authors’ implementation typically requires setting up an often complex development environment with matching package versions. In our experience, not all authors make this version information readily available, such that users may have to resort to trial and error. Additionally, the user’s hardware might not be on par with the authors’. If a network exhausts the memory of the user’s GPU, avoiding prohibitively long training times on the CPU necessitates reducing model capacity, which can affect performance. In principle, users could retrain DL methods despite these challenges. However, the burden is usually sufficiently large that users will turn to methods that distribute pre-trained models. For this reason, we specifically compare DL baselines pre-trained by the respective authors, to gauge the performance attainable without retraining. We hope the broad applicability of SynthMorph may help alleviate the historically limited reusability of DL methods.

5.5 Joint registration

The joint baseline comparison highlights that deformable algorithms cannot always fully compensate for real-world inaccuracies in affine initialization. Generally, the median Dice overlap drops by a few percent when we initialize each tool with affine transforms estimated by the same package instead of NiftyReg, the most accurate affine baseline tested. This experiment demonstrates the importance of accurate affine registration for joint accuracy—choosing affine and deformable algorithms from the same package is likely the most common use case.

In Section 4.5, the affine subnetwork of the 10-cascade VTN model consistently ranks among the least accurate methods even for the T1w image type it trained with. The authors of VTN do not independently compare the affine component to baselines and instead focus on joint affine-deformable accuracy (Zhao et al., 2019b,d). While the VTN publication presents the affine cascade as an Encoder architecture ($C = 1$, Section 3.3) terminating with an FC layer (Zhao et al., 2019d), the public implementation omits the FC layer (Zhao et al., 2019c). Some of our early experiments with this architecture indicated that the FC layer is critical to competitive performance.

5.6 An ill-posed problem

Compared to within-subject affine registration, cross-subject affine registration is an ill-defined optimization problem. The human cortex, for example, exhibits complex folding patterns that vary considerably between indi-

viduals, and transforms limited to translation, rotation, scaling, and shear can only establish a gross match between subjects. This implies that a transform maximizing NCC may not necessarily lead to optimal Dice scores, and vice versa. While the Dice coefficient is certainly not the ultimate measure of accuracy, many neuroimage registration studies assess anatomical overlap, since there is little argument where most volumetric borders are. Label-based losses may have a difficult optimization landscape when images are far apart, or when structures have no initial overlap. For example, our models did not converge when augmenting label maps across the full range of rotations $r_i \in [-180^\circ, 180^\circ]$ about any axis i .

5.7 Rotational range

At training, SynthMorph sees registration pairs rotated apart by angles in excess of $|r_i| = 90^\circ$ about any axis i , due to the combined effect of spatial augmentation (Table B.1) and the rotational offset already present between any two input label maps. This limits SynthMorph’s rotational range to just over half of the possible $|r_i| = 180^\circ$ range, considering voxel data alone. Although prior work (Yu et al., 2022) and the analysis of Section 4.4 demonstrate that with an NCC loss Detector can effectively capture rotations up to $|r_i| = 180^\circ$, medical applications will not typically require the full range. For example, the rotational ranges measured within OASIS and ABCD do not exceed $|r_i| \leq 43.1^\circ$ (Figure C.1). Even in situations where rotations up to $|r_i| \leq 180^\circ$ can occur, the registration problem reduces to an effective 45° range when transposing the moving image to match the fixed-image orientation based on the orientation information typically stored in medical image headers.

5.8 Degrees of freedom

While we estimate the full affine transformation matrix with 12 DOF in 3D space, some applications require fewer DOF. An example is the correction of head motion during neuroimaging with MRI (Gallichan et al., 2016; Tisdall et al., 2012; White et al., 2010), where the bulk motion and its possible mitigation through pulse-sequence adjustments are physically constrained to 6 DOF accounting for translation and rotation. Although our evaluation is limited to affine registration, the Detector architecture used by SynthMorph could support lower-DOF registration in several ways. First, the WLS problem (11) has closed-form solutions for various numbers of DOF, and prior work evaluated a 6-DOF model (Moyer et al., 2021). Second, we can decompose the affine matrix \hat{t} of Equation (9) into translation, rotation, scaling, and shearing parameters for each axis of space (Appendix A). Using a modified transform \hat{t}_{vr} in the loss (6)—reconstructed from translations v_i and rotation parameters r_i only—would encourage the network to detect features optimal for rigid alignment.

5.9 Future work

We plan to expand our work in several ways. First, we will provide a trained 6-DOF model for rigid registration, as many applications require translations and rotations only, and the most accurate rigid transform does not necessarily correspond to the translation and rotation encoded in the most accurate affine transform.

Second, we will employ the proposed strategy and affine architecture to train specialized models for within-subject registration for navigator-based motion correction of neuroimaging with MRI (Gallichan et al., 2016; Hoffmann et al., 2016; Tisdall et al., 2012; White et al., 2010). These models need to be efficient for real-time use but do not have to be invariant to MRI contrast or resolution when employed to track head-pose changes between navigators acquired with a fixed protocol. However, the brain-specific registration made possible by SynthMorph will improve motion tracking and correction in the presence of jaw movement (Hoffmann et al., 2020).

Third, another application that can dramatically benefit from anatomy-specific registration is fetal neuroimaging, where the fetal brain is surrounded by features such as amniotic fluid and maternal tissue. We plan to tackle registration of the fetal brain, which is challenging, partly due to its small size, and which currently relies on brain extraction prior to registration to remove confounding image content (Gaudfernau et al., 2021).

6 Conclusion

We present an easy-to-use DL tool for end-to-end registration of images right off the scanner, without any preprocessing. Our study demonstrates the feasibility of training accurate affine and joint registration networks that generalize to image types unseen at training, outperforming established baselines across a landscape of image contrasts and resolutions. In a rigorous analysis approximating the diversity of real-world data, we find that our networks achieve invariance to protocol-specific image characteristics by leveraging a strategy that synthesizes wildly variable training images from label maps.

Optimizing the spatial overlap of select anatomical labels enables anatomy-specific registration without the need for segmentation that removes distracting content from the input images. We believe this independence from complex preprocessing has great promise for time-critical applications, such as real-time motion correction of MRI. Importantly, SynthMorph is a widely applicable learning strategy for anatomy-aware and acquisition-agnostic registration of any anatomy with any network architecture, as long as label maps are available for training—there is no need for these at registration time.

Data and code availability

A stand-alone SynthMorph utility and the source code are available at <https://w3id.org/synthmorph>. We also distribute SynthMorph as part of the open-source FreeSurfer package at <https://freesurfer.net>. The experiments presented in this study retrospectively analyze public datasets whose original sources we indicate in Section 4.1.

Ethics

We retrospectively re-analyze public datasets only. The Mass General Brigham Internal Review Board (IRB) approved the FSM study and the infant study. The Committee on Clinical Investigation at Boston Children’s Hospital approved the infant study. Retrospective analysis of de-identified open-access data did not require ethical approval. All subjects gave written informed consent.

Author contributions

Malte Hoffmann worked on conceptualization, data curation, formal analysis, funding acquisition, investigation, methodology, project administration, software, writing (original draft, review, editing). Andrew Hoopes assisted with data curation, methodology, resources, software, validation, writing (review, editing). Douglas N. Greve helped with data curation, funding acquisition, resources, validation, writing (review, editing). Bruce Fischl worked on conceptualization, funding acquisition, investigation, methodology, resources, software, supervision, writing (review, editing). Adrian V. Dalca contributed to conceptualization, methodology, resources, software, supervision, writing (review, editing).

Acknowledgments

The authors thank Lilla Zöllei and OASIS Cross-Sectional for sharing data (PIs D. Marcus, R. Buckner, J. Csernansky, J. Morris, NIH awards P50 AG05681, P01 AG03991, P01 AG026276, R01 AG021910, P20 MH071616, U24 R021382). We are grateful for funding from the National Institute of Biomedical Imaging and Bioengineering (P41 EB015896, P41 EB030006, R01 EB019956, R01 EB023281, R01 EB033773, R21 EB018907), the National Institute of Child Health and Human Development (R00 HD101553), the National Institute on Aging (R01 AG016495, R01 AG070988, R21 AG082082, R56 AG064027), the National Institute of Mental Health (RF1 MH121885, RF1 MH123195), the National Institute of Neurological Disorders and Stroke (R01 NS070963, R01 NS083534, R01 NS105820, U01 NS132181, UM1 NS132358), and the National Center for Research Resources (S10 RR019307, S10 RR023043, S10 RR023401). We acknowledge additional support from the BRAIN

Initiative Cell Census Network (U01 MH117023) and the NIH Blueprint for Neuroscience Research (U01 MH093765), part of the multi-institutional Human Connectome Project. The study also benefited from computational hardware provided by the Massachusetts Life Sciences Center.

Declaration of interests

Bruce Fischl has financial interests in CorticoMetrics, a company whose medical pursuits focus on brain imaging and measurement technologies. Malte Hoffmann and Bruce Fischl receive salary support from GE HealthCare. Massachusetts General Hospital and Mass General Brigham manage this interest in accordance with their conflict of interest policies. The authors have no other interests that could have inappropriately influenced the work reported in this paper.

A Affine parameterization

Let f be a fixed ND image of side lengths d_i , where $i \in \{1, \dots, N\}$ indexes the right-handed axes of the spatial image domain Ω . This work uses zero-centered index voxel coordinates $x \in \Omega$. That is,

$$\Omega = \prod_{i=1}^N \left\{ -\Delta d_i, 1 - \Delta d_i, \dots, d_i - 1 - \Delta d_i \right\} \quad (\text{A.1})$$

with $\Delta d_i = (d_i - 1)/2$, placing the center of rotations at the center of f . Let $T : \Omega \rightarrow \mathbb{R}^N$ be the affine coordinate transform of Equation (1), which maps a moving image m onto the domain of f . We parameterize T as

$$T = VRZE, \quad (\text{A.2})$$

where V , R , Z , E are matrices describing translation, rotation, scaling, and shear, respectively. Denoting v_i the translation and z_i the scaling parameter along axis i , we define

$$V = \left(\begin{array}{ccc|c} & & & v_1 \\ & I_N & & \vdots \\ & & & v_N \\ \hline 0 & \dots & 0 & 1 \end{array} \right), \quad (\text{A.3})$$

and

$$Z = \left(\begin{array}{cccc} z_1 & & & \\ & \ddots & & \\ & & z_N & \\ & & & 1 \end{array} \right). \quad (\text{A.4})$$

For rotations and shear, we distinguish between the 2D and 3D case. Let r_i be the angle of rotation about axis i , where the direction of rotation follows the right-hand rule. We abbreviate $c_i = \cos(r_i)$ and $s_i = \sin(r_i)$.

A.1 Two-dimensional case

In 2D, we apply the rotation angle $r = r_3$ and shear e using matrices

$$R = \begin{pmatrix} c_3 & -s_3 & 0 \\ s_3 & c_3 & 0 \\ 0 & 0 & 1 \end{pmatrix}, \quad E = \begin{pmatrix} 1 & e & 0 \\ 0 & 1 & 0 \\ 0 & 0 & 1 \end{pmatrix}. \quad (\text{A.5})$$

A.2 Three-dimensional case

We consider intrinsic 3D rotations represented as the matrix product $R = R_1 R_2 R_3$, where

$$R_1 = \begin{pmatrix} 1 & 0 & 0 & 0 \\ 0 & c_1 & -s_1 & 0 \\ 0 & s_1 & c_1 & 0 \\ 0 & 0 & 0 & 1 \end{pmatrix}, \quad (\text{A.6})$$

$$R_2 = \begin{pmatrix} c_2 & 0 & s_2 & 0 \\ 0 & 1 & 0 & 0 \\ -s_2 & 0 & c_2 & 0 \\ 0 & 0 & 0 & 1 \end{pmatrix}, \quad (\text{A.7})$$

$$R_3 = \begin{pmatrix} c_3 & -s_3 & 0 & 0 \\ s_3 & c_3 & 0 & 0 \\ 0 & 0 & 1 & 0 \\ 0 & 0 & 0 & 1 \end{pmatrix}, \quad (\text{A.8})$$

and we apply the shears $\{e_i\}$ using the parameterization:

$$E = \begin{pmatrix} 1 & e_1 & e_2 & 0 \\ 0 & 1 & e_3 & 0 \\ 0 & 0 & 1 & 0 \\ 0 & 0 & 0 & 1 \end{pmatrix}. \quad (\text{A.9})$$

A.3 Transforming coordinates

With the notation introduced in Equation (1), we transform the coordinates of an ND point

$$x = (x_1 \ x_2 \ \dots \ x_N)^\top \in \Omega \quad (\text{A.10})$$

as $x' = Ax + v$, or, using a single matrix product,

$$\begin{pmatrix} x' \\ \hline 1 \end{pmatrix} = T \begin{pmatrix} x \\ \hline 1 \end{pmatrix}. \quad (\text{A.11})$$

B Generation hyperparameters

Table B.1 lists the generation hyperparameters ranges that SynthMorph training uses for label-map augmentation and image synthesis.

Table B.1. Uniform hyperparameter sampling ranges $[a, b]$ for synthesizing training images from source segmentation maps. We abbreviate standard deviation (SD), full width at half maximum (FWHM), and field of view (FOV).

Hyperparameter	Unit	a	b
Translation	mm	-30	30
Rotation	°	-45	45
Scaling	%	90	110
Shear	%	90	110
Warp sampling SD	mm	0	4
Warp blurring FWHM	mm	8	32
Label intensity mean	a.u.	0	1
Noise intensity SD	%	3	10
Image blurring FWHM	mm	0	8
Bias field sampling SD	%	0	10
Bias field blurring FWHM	mm	48	64
FOV cropping	%	0	20
Downsampling factor	%	1	8
Gamma exponent	-	0.5	1.5

C Transform analysis

In this supplementary experiment, we analyze the range of typical transforms a registration tool may have to cope with. We register 1000 distinct and randomly pooled subject pairs from OASIS and another 1000 pairs from ABCD. The estimated transformation matrix T decomposes into the translation, rotation, scaling, and shearing parameters defined in Appendix A.

Figure C.1 presents the range of absolute transformation parameters measured within OASIS and ABCD, along any axis $i \in \{1, 2, 3\}$ of the space introduced in Section 4.1. Within OASIS, the mean translations and rotations are $\overline{|v_i|} = (8.5 \pm 9.9)$ mm and $\overline{|r_i|} = (5.6 \pm 6.0)^\circ$, respectively (\pm standard deviation, SD).

The average scaling and shearing parameters are $\overline{|z_i - 1|} = (5.0 \pm 3.8)\%$ and $\overline{|e_i|} = (3.3 \pm 3.0)\%$, respectively. While most transforms are small, a subset of the OASIS subjects are far apart, leading to large total ranges of translation $|v_i| \leq 61.1$ mm, rotation $|r_i| \leq 43.1^\circ$, scaling $|z_i - 1| \leq 22.6\%$, and shear $|e_i| \leq 22.1\%$. Transforms within ABCD follow a similar distribution.

Therefore, we choose to augment input label maps at training with affine transforms drawn from the ranges of Table B.1, ensuring that SynthMorph covers the transformation parameters measured across public datasets.

References

Fidel Alfaro-Almagro, Mark Jenkinson, Neal K Bangerter, Jesper LR Andersson, Ludovica Griffanti, Gwenaëlle Douaud, Stamatios N Sotiropoulos, Saad Jbabdi, Moises Hernandez-Fernandez, Emmanuel Vallee, et al. Image processing and Quality Control for the first 10,000 brain imaging datasets from UK Biobank. *NeuroImage*, 166:400–424, 2018.

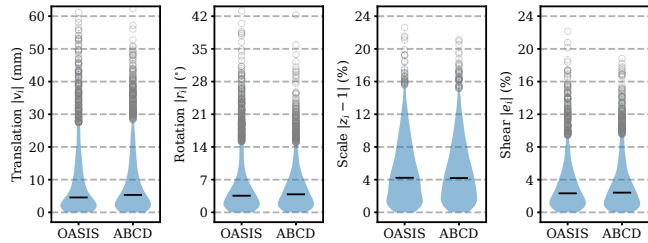


Figure C.1. Absolute affine transformation range across $n = 1000$ registration pairs randomly selected from either OASIS or ABCD. Each panel pools parameters relative to all axes $i \in \{1, 2, 3\}$ of 3D space. Black bars indicate median values. Circles represent parameters farther than 1.5 inter-quartile ranges from the median.

Jesper LR Andersson, Mark Jenkinson, Stephen Smith, et al. Non-linear registration, aka spatial normalisation fmrib technical report tr07ja2. *FMRIB Analysis Group of the University of Oxford*, 2(1):e21, 2007.

Natan Andrade, Fabio Augusto Faria, and Fábio Augusto Menocci Cappabianco. A practical review on medical image registration: From rigid to deep learning based approaches. In *2018 31st SIBGRAPI Conference on Graphics, Patterns and Images (SIBGRAPI)*, pages 463–470. IEEE, 2018.

John Ashburner. A fast diffeomorphic image registration algorithm. *NeuroImage*, 38(1):95–113, 2007.

John Ashburner and Karl J Friston. Voxel-based morphometry—the methods. *NeuroImage*, 11(6):805–821, 2000.

Brian B Avants, Charles L Epstein, Murray Grossman, and James C Gee. Symmetric diffeomorphic image registration with cross-correlation: evaluating automated labeling of elderly and neurodegenerative brain. *Medical Image Analysis*, 12(1):26–41, 2008.

Brian B Avants, Nicholas J Tustison, Gang Song, Philip A Cook, Arno Klein, and James C Gee. A reproducible evaluation of ANTs similarity metric performance in brain image registration. *NeuroImage*, 54(3):2033–2044, 2011.

Guha Balakrishnan, Amy Zhao, Mert Sabuncu, John Guttag, and Adrian V. Dalca. VoxelMorph: A Learning Framework for Deformable Medical Image Registration. *IEEE Transactions on Medical Imaging*, 38(8):1788–1800, 2019.

Paul J Besl and Neil D McKay. Method for registration of 3-D shapes. In *Sensor fusion IV: control paradigms and data structures*, volume 1611, pages 586–606. SPIE, 1992.

Seth D Billings, Emad M Boctor, and Russell H Taylor. Iterative most-likely point registration (IMLP): A robust algorithm for computing optimal shape alignment. *PLOS One*, 10(3):e0117688, 2015.

- Benjamin Billot, Douglas N Greve, Koen Van Leemput, Bruce Fischl, Juan Eugenio Iglesias, and Adrian Dalca. A Learning Strategy for Contrast-agnostic MRI Segmentation. In *Medical Imaging with Deep Learning*, pages 75–93. PMLR, 2020.
- Fred L Bookstein. “Voxel-based morphometry” should not be used with imperfectly registered images. *NeuroImage*, 14(6):1454–1462, 2001.
- Leon Y Cai, Qi Yang, Praitayini Kanakaraj, Vishwesh Nath, Allen T Newton, Heidi A Edmonson, Jeffrey Luci, Benjamin N Conrad, Gavin R Price, Colin B Hansen, et al. MASiVar: Multisite, multiscanner, and multisubject acquisitions for studying variability in diffusion weighted MRI. *Magnetic Resonance in Medicine*, 86(6):3304–3320, 2021.
- BJ Casey, Tariq Cannonier, May I Conley, Alexandra O Cohen, Deanna M Barch, Mary M Heitzeg, Mary E Soules, Theresa Teslovich, Danielle V Dellarco, Hugh Garavan, et al. The adolescent brain cognitive development (ABCD) study: imaging acquisition across 21 sites. *Developmental Cognitive Neuroscience*, 32:43–54, 2018.
- Krishna Chaitanya, Neerav Karani, Christian F Baumgartner, Anton Becker, Olivio Donati, and Ender Konukoglu. Semi-supervised and task-driven data augmentation. In *International Conference on Information Processing in Medical Imaging*, pages 29–41. Springer, 2019.
- Min Chen, Aaron Carass, Amod Jog, Junghoon Lee, Snehashis Roy, and Jerry L Prince. Cross contrast multi-channel image registration using image synthesis for MR brain images. *Medical Image Analysis*, 36:2–14, 2017.
- Xu Chen, Yanda Meng, Yitian Zhao, Rachel Williams, Srinivasa R Vallabhaneni, and Yalin Zheng. Learning Unsupervised Parameter-Specific Affine Transformation for Medical Images Registration. In *International Conference on Medical Image Computing and Computer-Assisted Intervention*, pages 24–34. Springer, 2021.
- Kenneth Clark, Bruce Vendt, Kirk Smith, John Freymann, Justin Kirby, Paul Koppel, Stephen Moore, Stanley Phillips, David Maffitt, Michael Pringle, et al. The Cancer Imaging Archive (TCIA): maintaining and operating a public information repository. *Journal of digital imaging*, 26(6):1045–1057, 2013.
- Robert W Cox. AFNI: software for analysis and visualization of functional magnetic resonance neuroimages. *Computers and Biomedical Research*, 29(3):162–173, 1996.
- Robert W Cox and Andrzej Jesmanowicz. Real-time 3D image registration for functional MRI. *Magnetic Resonance in Medicine*, 42(6):1014–1018, 1999.
- Adrian Dalca, Marianne Rakic, John Guttag, and Mert Sabuncu. Learning conditional deformable templates with convolutional networks. *Advances in Neural Information Processing Systems*, 32, 2019a.
- Adrian V Dalca, Guha Balakrishnan, John Guttag, and Mert R Sabuncu. Unsupervised learning for fast probabilistic diffeomorphic registration. In *International Conference on Medical Image Computing and Computer-Assisted Intervention*, pages 729–738. Springer, 2018.
- Adrian V. Dalca, Guha Balakrishnan, John Guttag, and Mert Sabuncu. Unsupervised Learning of Probabilistic Diffeomorphic Registration for Images and Surfaces. *Medical Image Analysis*, 57:226–236, 2019b.
- Katyucia de Macedo Rodrigues, Emma Ben-Avi, Danielle D Sliva, Myong-sun Choe, Marie Drottar, Ruopeng Wang, Bruce Fischl, Patricia E Grant, and Lilla Zöllei. A FreeSurfer-compliant consistent manual segmentation of infant brains spanning the 0–2 year age range. *Frontiers in Human Neuroscience*, 9:21, 2015.
- Bob D de Vos, Floris F Berendsen, Max A Viergever, Marius Staring, and Ivana Išgum. End-to-end unsupervised deformable image registration with a convolutional neural network. In *DLMIA*, pages 204–212. Springer, 2017.
- Bob D De Vos, Floris F Berendsen, Max A Viergever, Hessam Sokooti, Marius Staring, and Ivana Išgum. A deep learning framework for unsupervised affine and deformable image registration. *Medical Image Analysis*, 52:128–143, 2019.
- Lee R Dice. Measures of the amount of ecologic association between species. *Ecology*, 26(3):297–302, 1945.
- Xiaohan Ding, Xiangyu Zhang, Jungong Han, and Guiguang Ding. Scaling up your kernels to 31x31: Revisiting large kernel design in cnns. In *Proceedings of the IEEE/CVF Conference on Computer Vision and Pattern Recognition*, pages 11963–11975, 2022.
- Zhipeng Ding and Marc Niethammer. Aladdin: Joint Atlas Building and Diffeomorphic Registration Learning with Pairwise Alignment. *arXiv preprint arXiv:2202.03563*, 2022.
- Alexey Dosovitskiy, Lucas Beyer, Alexander Kolesnikov, Dirk Weissenborn, Xiaohua Zhai, Thomas Unterthiner, Mostafa Dehghani, Matthias Minderer, Georg Heigold, Sylvain Gelly, et al. An image is worth 16x16 words: Transformers for image recognition at scale. *arXiv preprint arXiv:2010.11929*, 2020.

- K. A. J. Eppenhof and J. P. W. Pluim. Pulmonary CT registration through supervised learning with convolutional neural networks. *IEEE Transactions on Medical Imaging*, 38(5):1097–1105, 2019.
- Simon F Eskildsen, Pierrick Coupé, Vladimir Fonov, José V Manjón, Kelvin K Leung, Nicolas Guizard, Shafik N Wassef, Lasse Riis Østergaard, D Louis Collins, Alzheimer’s Disease Neuroimaging Initiative, et al. BEaST: brain extraction based on nonlocal segmentation technique. *NeuroImage*, 59(3):2362–2373, 2012.
- George Fein, Bennett Landman, Hoang Tran, Jerome Barakos, Kirk Moon, Victoria Di Sclafani, and Robert Shumway. Statistical parametric mapping of brain morphology: sensitivity is dramatically increased by using brain-extracted images as inputs. *NeuroImage*, 30(4):1187–1195, 2006.
- Bruce Fischl. FreeSurfer. *NeuroImage*, 62(2):774–781, 2012. ISSN 1053-8119. 20 YEARS OF fMRI.
- Bruce Fischl, David H Salat, Evelina Busa, Marilyn Albert, Megan Dieterich, Christian Haselgrove, Andre Van Der Kouwe, Ron Killiany, David Kennedy, Shuna Klaveness, et al. Whole brain segmentation: automated labeling of neuroanatomical structures in the human brain. *Neuron*, 33(3):341–355, 2002.
- Bruce Fischl, David H Salat, André JW Van Der Kouwe, Nikos Makris, Florent Ségonne, Brian T Quinn, and Anders M Dale. Sequence-independent segmentation of magnetic resonance images. *NeuroImage*, 23:S69–S84, 2004.
- F Ph S Fischmeister, I Höllinger, N Klinger, A Geissler, MC Wurnig, E Matt, J Rath, SD Robinson, S Trattning, and R Beisteiner. The benefits of skull stripping in the normalization of clinical fMRI data. *NeuroImage: Clinical*, 3:369–380, 2013.
- Karl J Friston, John Ashburner, Christopher D Frith, J-B Poline, John D Heather, and Richard SJ Frackowiak. Spatial registration and normalization of images. *Human Brain Mapping*, 3(3):165–189, 1995.
- Yabo Fu, Yang Lei, Tonghe Wang, Walter J Curran, Tian Liu, and Xiaofeng Yang. Deep learning in medical image registration: a review. *Physics in Medicine & Biology*, 65(20):20TR01, 2020.
- Daniel Gallichan, José P Marques, and Rolf Grueter. Retrospective correction of involuntary microscopic head movement using highly accelerated fat image navigators (3D FatNavs) at 7T. *Magnetic Resonance in Medicine*, 75(3):1030–1039, 2016.
- Fleur Gaudfernau, Eléonore Blondiaux, and Stéphanie Allassonnière. Analysis of the Anatomical Variability of Fetal Brains with Corpus Callosum Agenesis. In *Uncertainty for Safe Utilization of Machine Learning in Medical Imaging, and Perinatal Imaging, Placental and Preterm Image Analysis*, pages 274–283, Cham, 2021. Springer.
- Natasha Gelfand, Niloy J Mitra, Leonidas J Guibas, and Helmut Pottmann. Robust global registration. In *Symposium on Geometry Processing*, volume 2, page 5. Eurographics, 2005.
- Ben Glocker, Nikos Komodakis, Georgios Tziritas, Nassir Navab, and Nikos Paragios. Dense image registration through mrfs and efficient linear programming. *Medical image analysis*, 12(6):731–741, 2008.
- Ben Glocker, Aristeidis Sotiras, Nikos Komodakis, and Nikos Paragios. Deformable medical image registration: setting the state of the art with discrete methods. *Annual review of biomedical engineering*, 13:219–244, 2011.
- Douglas N Greve, Benjamin Billot, Devani Cordero, Andrew Hoopes, Malte Hoffmann, Adrian V Dalca, Bruce Fischl, Juan Eugenio Iglesias, and Jean C Augustinack. A deep learning toolbox for automatic segmentation of subcortical limbic structures from MRI images. *NeuroImage*, 244:118610, 2021.
- Courtney K Guo. *Multi-modal image registration with unsupervised deep learning*. PhD thesis, Massachusetts Institute of Technology, 2019.
- Joseph V Hajnal and Derek LG Hill. *Medical image registration*. CRC Press, 2001.
- Michael P. Harms et al. Extending the Human Connectome Project across ages: Imaging protocols for the Lifespan Development and Aging projects. *NeuroImage*, 183:972–984, 2018. ISSN 1053-8119.
- Mattias P Heinrich. Closing the gap between deep and conventional image registration using probabilistic dense displacement networks. In *Medical Image Computing and Computer Assisted Intervention—MICCAI 2019: 22nd International Conference, Shenzhen, China, October 13–17, 2019, Proceedings, Part VI 22*, pages 50–58. Springer, 2019.
- Mattias P Heinrich, Mark Jenkinson, Manav Bhushan, Tahreema Matin, Fergus V Gleeson, Michael Brady, and Julia A Schnabel. MIND: Modality independent neighbourhood descriptor for multi-modal deformable registration. *Medical Image Analysis*, 16(7):1423–1435, 2012.
- Mattias P Heinrich, Mark Jenkinson, Michael Brady, and Julia A Schnabel. MRF-based deformable registration and ventilation estimation of lung CT. *IEEE Transactions on Medical Imaging*, 32(7):1239–1248, 2013.

- Pierre Hellier, Christian Barillot, Etienne Mémin, and Patrick Pérez. Hierarchical estimation of a dense deformation field for 3-D robust registration. *IEEE Transactions on Medical Imaging*, 20(5):388–402, 2001.
- Malte Hoffmann, T Adrian Carpenter, Guy B Williams, and Stephen J Sawiak. A survey of patient motion in disorders of consciousness and optimization of its retrospective correction. *Magnetic Resonance Imaging*, 33(3):346–350, 2015.
- Malte Hoffmann, Marius Mada, T Adrian Carpenter, Stephen J Sawiak, and Guy B Williams. Additional sampling directions improve detection range of wireless radiofrequency probes. *Magnetic Resonance in Medicine*, 76(3):913–918, 2016.
- Malte Hoffmann, Robert Frost, David Salat, M Dylan Tisdall, Jonathan Polimeni, and André van der Kouwe. Real-time brain masking algorithm improves motion tracking accuracy in scans with volumetric navigators (vNavs). In *Proceedings of the 28th Annual Meeting of ISMRM*, page 3367. ISMRM, 2020.
- Malte Hoffmann, Benjamin Billot, Douglas N Greve, Juan Eugenio Iglesias, Bruce Fischl, and Adrian V Dalca. SynthMorph: learning contrast-invariant registration without acquired images. *IEEE Transactions on Medical Imaging*, 2021a.
- Malte Hoffmann, Benjamin Billot, Juan E Iglesias, Bruce Fischl, and Adrian V Dalca. Learning MRI contrast-agnostic registration. In *2021 IEEE 18th International Symposium on Biomedical Imaging (ISBI)*, pages 899–903. IEEE, 2021b.
- Malte Hoffmann, Andrew Hoopes, Bruce Fischl, and Adrian V Dalca. Anatomy-specific acquisition-agnostic affine registration learned from fictitious images. In *Medical Imaging 2023: Image Processing*, volume 12464, page 1246402. SPIE, 2023.
- Avram J Holmes, Marisa O Hollinshead, Timothy M O’keefe, Victor I Petrov, Gabriele R Fariello, Lawrence L Wald, Bruce Fischl, Bruce R Rosen, Ross W Mair, Joshua L Roffman, et al. Brain Genomics Superstruct Project initial data release with structural, functional, and behavioral measures. *Scientific Data*, 2(1):1–16, 2015.
- Andrew Hoopes, Malte Hoffmann, Douglas N Greve, Bruce Fischl, John Guttag, Adrian V Dalca, et al. Learning the effect of registration hyperparameters with hypermorph. *Machine Learning for Biomedical Imaging*, 1(IPMI 2021 special issue):1–30, 2022a.
- Andrew Hoopes, Jocelyn S Mora, Adrian V Dalca, Bruce Fischl, and Malte Hoffmann. SynthStrip: skull-stripping for any brain image. *NeuroImage*, 260:119474, 2022b. ISSN 1053-8119. doi: <https://doi.org/10.1016/j.neuroimage.2022.119474>.
- Yipeng Hu, Marc Modat, Eli Gibson, Nooshin Ghavami, Ester Bonmati, Caroline M Moore, Mark Emberton, J Alison Noble, Dean C Barratt, and Tom Vercauteren. Label-driven weakly-supervised learning for multimodal deformable image registration. In *2018 IEEE 15th International Symposium on Biomedical Imaging (ISBI 2018)*, pages 1070–1074. IEEE, 2018.
- Juan Eugenio Iglesias, Cheng-Yi Liu, Paul M Thompson, and Zhuowen Tu. Robust brain extraction across datasets and comparison with publicly available methods. *IEEE Transactions on Medical Imaging*, 30(9):1617–1634, 2011.
- Juan Eugenio Iglesias, Ender Konukoglu, Darko Zikic, Ben Glocker, Koen Van Leemput, and Bruce Fischl. Is synthesizing MRI contrast useful for inter-modality analysis? In *International Conference on Medical Image Computing and Computer-Assisted Intervention*, pages 631–638. Springer, 2013.
- Imperial College London. IXI Dataset, 2015. URL <https://brain-development.org/ixi-dataset/>.
- Mark Jenkinson and Stephen Smith. A global optimisation method for robust affine registration of brain images. *Medical Image Analysis*, 5(2):143–156, 2001.
- Mark Jenkinson, Christian F Beckmann, Timothy EJ Behrens, Mark W Woolrich, and Stephen M Smith. Fsl. *NeuroImage*, 62(2):782–790, 2012.
- Aiping Jiang, David N Kennedy, John R Baker, Robert M Weisskoff, Roger BH Tootell, Roger P Woods, Randall R Benson, Kenneth K Kwong, Thomas J Brady, Bruce R Rosen, et al. Motion detection and correction in functional MR imaging. *Human Brain Mapping*, 3(3):224–235, 1995.
- Konstantinos Kamnitsas, Christian Baumgartner, Christian Ledig, Virginia Newcombe, Joanna Simpson, Andrew Kane, David Menon, Aditya Nori, Antonio Criminisi, Daniel Rueckert, et al. Unsupervised domain adaptation in brain lesion segmentation with adversarial networks. In *International Conference on Information Processing in Medical Imaging*, pages 597–609. Springer, 2017.
- Diederik P Kingma and Jimmy Ba. Adam: A method for stochastic optimization. *arXiv preprint arXiv:1412.6980*, 2014.
- Arno Klein, Jesper Andersson, Babak A Ardekani, John Ashburner, Brian Avants, Ming-Chang Chiang, Gary E Christensen, D Louis Collins, James Gee, Pierre Hellier, et al. Evaluation of 14 nonlinear deformation algorithms applied to human brain MRI registration. *NeuroImage*, 46(3):786–802, 2009.
- JB Kneeland, A Shimakawa, and FW Wehrli. Effect of intersection spacing on MR image contrast and study time. *Radiology*, 158(3):819–822, 1986.

- Julian Krebs, Tommaso Mansi, Hervé Delingette, Li Zhang, Florin C Ghesu, Shun Miao, Andreas K Maier, Nicholas Ayache, Rui Liao, and Ali Kamen. Robust non-rigid registration through agent-based action learning. In *International Conference on Medical Image Computing and Computer-Assisted Intervention*, pages 344–352, 2017.
- Julian Krebs, Hervé Delingette, Boris Mailhé, Nicholas Ayache, and Tommaso Mansi. Learning a probabilistic model for diffeomorphic registration. *IEEE Transactions on Medical Imaging*, 38(9):2165–2176, 2019.
- Hongming Li and Yong Fan. Non-rigid image registration using fully convolutional networks with deep self-supervision. *arXiv preprint arXiv:1709.00799*, 2017.
- Shiwei Liu, Tianlong Chen, Xiaohan Chen, Xuxi Chen, Qiao Xiao, Boqian Wu, Mykola Pechenizkiy, Decebal Mocanu, and Zhangyang Wang. More convnets in the 2020s: Scaling up kernels beyond 51x51 using sparsity. *arXiv preprint arXiv:2207.03620*, 2022a.
- Zhuang Liu, Hanzi Mao, Chao-Yuan Wu, Christoph Feichtenhofer, Trevor Darrell, and Saining Xie. A convnet for the 2020s. In *Proceedings of the IEEE/CVF Conference on Computer Vision and Pattern Recognition*, pages 11976–11986, 2022b.
- M. Lorenzi, N. Ayache, G.B. Frisoni, and X. Pennec. LCC-Demons: A robust and accurate symmetric diffeomorphic registration algorithm. *NeuroImage*, 81:470–483, 2013. ISSN 1053-8119.
- David G Lowe. Distinctive image features from scale-invariant keypoints. *International Journal of Computer Vision*, 60(2):91–110, 2004.
- Inês Machado, Matthew Toews, Jie Luo, Prashin Unadkat, Walid Essayed, Elizabeth George, Pedro Teodoro, Herculano Carvalho, Jorge Martins, Polina Golland, et al. Non-rigid registration of 3D ultrasound for neurosurgery using automatic feature detection and matching. *International Journal of Computer Assisted Radiology and Surgery*, 13(10):1525–1538, 2018.
- Frederik Maes, Andre Collignon, Dirk Vandermeulen, Guy Marchal, and Paul Suetens. Multimodality image registration by maximization of mutual information. *IEEE Transactions on Medical Imaging*, 16(2):187–198, 1997.
- AB Mamonov and J Kalpathy-Cramer. Data From QIN GBM Treatment Response, 2016.
- Daniel S Marcus, Tracy H Wang, Jamie Parker, John G Csernansky, John C Morris, and Randy L Buckner. Open access series of imaging studies (oasis): cross-sectional MRI data in young, middle aged, nondemented, and demented older adults. *Journal of Cognitive Neuroscience*, 19(9):1498–1507, 2007.
- Jiri Matas, Ondrej Chum, Martin Urban, and Tomás Pajdla. Robust wide-baseline stereo from maximally stable extremal regions. *Image and Vision Computing*, 22(10):761–767, 2004.
- Charles R Meyer, Gregg S Leichtman, James A Brunberg, Richard L Wahl, and Leslie E Quint. Simultaneous usage of homologous points, lines, and planes for optimal, 3-D, linear registration of multimodality imaging data. *IEEE Transactions on Medical Imaging*, 14(1):1–11, 1995.
- Karla L Miller, Fidel Alfaro-Almagro, Neal K Bangerter, David L Thomas, Essa Yacoub, Junqian Xu, Andreas J Bartsch, Saad Jbabdi, Stamatios N Sotiropoulos, Jesper LR Andersson, et al. Multimodal population brain imaging in the uk biobank prospective epidemiological study. *Nature neuroscience*, 19(11):1523–1536, 2016.
- Fausto Milletari, Nassir Navab, and Seyed-Ahmad Ahmadi. V-net: Fully convolutional neural networks for volumetric medical image segmentation. In *2016 4th International Conference on 3D Vision (3DV)*, pages 565–571. IEEE, 2016.
- Marc Modat, David M Cash, Pankaj Daga, Gavin P Winston, John S Duncan, and Sébastien Ourselin. Global image registration using a symmetric block-matching approach. *Journal of Medical Imaging*, 1(2):024003, 2014.
- Tony C. W. Mok and Albert C. S. Chung. Affine Medical Image Registration with Coarse-to-Fine Vision Transformer. *arXiv preprint arXiv:2203.15216*, 2022.
- Daniel Moyer, Esra Abaci Turk, P Ellen Grant, William M Wells, and Polina Golland. Equivariant Filters for Efficient Tracking in 3D Imaging. In *International Conference on Medical Image Computing and Computer-Assisted Intervention*, pages 193–202. Springer, 2021.
- Andriy Myronenko and Xubo Song. Point set registration: Coherent point drift. *IEEE Transactions on Pattern Analysis and Machine Intelligence*, 32(12):2262–2275, 2010.
- Oscar Nestares and David J Heeger. Robust multiresolution alignment of MRI brain volumes. *Magnetic Resonance in Medicine*, 43(5):705–715, 2000.
- Francisco PM Oliveira and Joao Manuel RS Tavares. Medical image registration: a review. *Computer Methods in Biomechanics and Biomedical Engineering*, 17(2):73–93, 2014.
- Yangming Ou, Aristeidis Sotiras, Nikos Paragios, and Christos Davatzikos. Dramms: Deformable registration via attribute matching and mutual-saliency weighting. *Medical image analysis*, 15(4):622–639, 2011.

- Yangming Ou, Hamed Akbari, Michel Bilello, Xiao Da, and Christos Davatzikos. Comparative evaluation of registration algorithms in different brain databases with varying difficulty: results and insights. *IEEE Transactions on Medical Imaging*, 33(10):2039–2065, 2014.
- Luis Perez and Jason Wang. The effectiveness of data augmentation in image classification using deep learning. *arXiv preprint arXiv:1712.04621*, 2017.
- Francesco Pinto, Philip HS Torr, and Puneet K Dokania. An impartial take to the cnn vs transformer robustness contest. In *European Conference on Computer Vision*, pages 466–480. Springer, 2022.
- MA Prah, SM Stufflebeam, ES Paulson, J Kalpathy-Cramer, ER Gerstner, TT Batchelor, DP Barboriak, BR Rosen, and KM Schmainda. Repeatability of standardized and normalized relative CBV in patients with newly diagnosed glioblastoma. *American Journal of Neuroradiology*, 36(9):1654–1661, 2015.
- Giovanni Puglisi and Sebastiano Battiato. A robust image alignment algorithm for video stabilization purposes. *IEEE Transactions on Circuits and Systems for Video Technology*, 21(10):1390–1400, 2011.
- Dorian Pustina and Philip Cook. Anatomy of an antsRegistration call, 2017. URL <https://github.com/ANTsX/ANTs/wiki/Anatomy-of-an-antsRegistration-call>.
- Chen Qin, Bibo Shi, Rui Liao, Tommaso Mansi, Daniel Rueckert, and Ali Kamen. Unsupervised deformable registration for multi-modal images via disentangled representations. In *International Conference on Information Processing in Medical Imaging*, pages 249–261. Springer, 2019.
- Martin Reuter, H. Diana Rosas, and Bruce Fischl. Highly accurate inverse consistent registration: A robust approach. *NeuroImage*, 53(4):1181–1196, 2010. ISSN 1053-8119.
- Blaine Rister, Mark A Horowitz, and Daniel L Rubin. Volumetric image registration from invariant keypoints. *IEEE Transactions on Image Processing*, 26(10):4900–4910, 2017.
- Alexis Roche, Grégoire Malandain, Xavier Pennec, and Nicholas Ayache. The correlation ratio as a new similarity measure for multimodal image registration. In *International Conference on Medical Image Computing and Computer-Assisted Intervention*, pages 1115–1124. Springer, 1998.
- Marc Rohé, Manasi Datar, Tobias Heimann, Maxime Sermesant, and Xavier Pennec. SVF-Net: Learning deformable image registration using shape matching. *International Conference on Medical Image Computing and Computer-Assisted Intervention*, pages 266–274, 2017.
- Torsten Rohlfing. Image similarity and tissue overlaps as surrogates for image registration accuracy: widely used but unreliable. *IEEE transactions on medical imaging*, 31(2):153–163, 2011.
- Karl Rohr, H Siegfried Stiehl, Rainer Sprengel, Thorsten M Buzug, Jürgen Weese, and MH Kuhn. Landmark-based elastic registration using approximating thin-plate splines. *IEEE Transactions on Medical Imaging*, 20(6):526–534, 2001.
- Olaf Ronneberger, Philipp Fischer, and Thomas Brox. U-net: Convolutional networks for biomedical image segmentation. In *International Conference on Medical Image Computing and Computer-Assisted Intervention*, pages 234–241. Springer, 2015.
- Daniel Rueckert, Luke I Sonoda, Carmel Hayes, Derek LG Hill, Martin O Leach, and David J Hawkes. Nonrigid registration using free-form deformations: application to breast MR images. *IEEE Transactions on Medical Imaging*, 18(8):712–721, 1999.
- Seyed Sadegh Mohseni Salehi, Deniz Erdogmus, and Ali Gholipour. Auto-context convolutional neural network (auto-net) for brain extraction in magnetic resonance imaging. *IEEE Transactions on Medical Imaging*, 36(11):2319–2330, 2017.
- Zhengyang Shen, Xu Han, Zhenlin Xu, and Marc Niethammer. Networks for joint affine and non-parametric image registration. In *Proceedings of the IEEE/CVF Conference on Computer Vision and Pattern Recognition*, pages 4224–4233, 2019.
- Connor Shorten and Taghi M Khoshgoftaar. A survey on image data augmentation for deep learning. *Journal of Big Data*, 6(1):1–48, 2019.
- Andrew Simmons, Paul S Tofts, Gareth J Barker, and Simon R Arridge. Sources of intensity nonuniformity in spin echo images at 1.5 T. *Magnetic Resonance in Medicine*, 32(1):121–128, 1994.
- Matthew Sinclair, Andreas Schuh, Karl Hahn, Kersten Petersen, Ying Bai, James Batten, Michiel Schaap, and Ben Glocker. Atlas-ISTN: joint segmentation, registration and atlas construction with image-and-spatial transformer networks. *Medical Image Analysis*, 78:102383, 2022.
- Stephen M Smith. Fast robust automated brain extraction. *Human Brain Mapping*, 17(3):143–155, 2002.
- Hessam Sokooti, Bob de Vos, Floris Berendsen, Boudewijn PF Lelieveldt, Ivana Išgum, and Marius Staring. Nonrigid image registration using multi-scale 3D convolutional neural networks. In *International Conference on Medical Image Computing and Computer-Assisted Intervention*, pages 232–239. Springer, 2017.

- Leah H Somerville, Susan Y Bookheimer, Randy L Buckner, Gregory C Burgess, Sandra W Curtiss, Mirella Dapretto, Jennifer Stine Elam, Michael S Gaffrey, Michael P Harms, Cynthia Hodge, et al. The Lifespan Human Connectome Project in Development: A large-scale study of brain connectivity development in 5–21 year olds. *NeuroImage*, 183:456–468, 2018.
- Cathie Sudlow, John Gallacher, Naomi Allen, Valerie Beal, Paul Burton, John Danesh, Paul Downey, Paul Elliott, Jane Green, Martin Landray, et al. UK biobank: an open access resource for identifying the causes of a wide range of complex diseases of middle and old age. *PLOS Medicine*, 12(3):e1001779, 2015.
- Baochen Sun, Jiashi Feng, and Kate Saenko. Return of frustratingly easy domain adaptation. In *Proceedings of the AAAI Conference on Artificial Intelligence*, volume 30, 2016.
- Christine Tanner, Firat Ozdemir, Romy Profanter, Valeriy Vishnevsky, Ender Konukoglu, and Orcun Goksel. Generative adversarial networks for MR-CT deformable image registration. *arXiv preprint arXiv:1807.07349*, 2018.
- Stefan Thesen, Oliver Heid, Edgar Mueller, and Lothar R Schad. Prospective acquisition correction for head motion with image-based tracking for real-time fMRI. *Magnetic Resonance in Medicine*, 44(3):457–465, 2000.
- M Dylan Tisdall, Aaron T Hess, Martin Reuter, Ernesta M Meintjes, Bruce Fischl, and André JW van der Kouwe. Volumetric navigators for prospective motion correction and selective reacquisition in neuroanatomical MRI. *Magnetic Resonance in Medicine*, 68(2):389–399, 2012.
- Matthew Toews and William M Wells III. Efficient and robust model-to-image alignment using 3D scale-invariant features. *Medical Image Analysis*, 17(3):271–282, 2013.
- Nicholas J Tustison, Brian B Avants, Philip A Cook, Gang Song, Sandhitsu Das, Niels van Strien, James R Stone, and James C Gee. The ANTs cortical thickness processing pipeline. In *Medical Imaging 2013: Biomedical Applications in Molecular, Structural, and Functional Imaging*, volume 8672, pages 126–129. SPIE, 2013.
- Christian Wachinger and Nassir Navab. Structural image representation for image registration. In *2010 IEEE Computer Society Conference on Computer Vision and Pattern Recognition-Workshops*, pages 23–30. IEEE, 2010.
- Christian Wachinger and Nassir Navab. Entropy and Laplacian images: Structural representations for multimodal registration. *Medical Image Analysis*, 16(1):1–17, 2012.
- Christian Wachinger, Matthew Toews, Georg Langs, William Wells, and Polina Golland. Keypoint transfer for fast whole-body segmentation. *IEEE Transactions on Medical Imaging*, 39(2):273–282, 2018.
- Mei Wang and Weihong Deng. Deep visual domain adaptation: A survey. *Neurocomputing*, 312:135–153, 2018.
- Yiqian Wang, Junkang Zhang, Melina Cavichini, Dirk-Uwe G Bartsch, William R Freeman, Truong Q Nguyen, and Cheolhong An. Robust content-adaptive global registration for multimodal retinal images using weakly supervised deep-learning framework. *IEEE Transactions on Image Processing*, 30:3167–3178, 2021.
- William M Wells III, Paul Viola, Hideki Atsumi, Shin Nakajima, and Ron Kikinis. Multi-modal volume registration by maximization of mutual information. *Medical Image Analysis*, 1(1):35–51, 1996.
- Nathan White, Cooper Roddey, Ajit Shankaranarayanan, Eric Han, Dan Rettmann, Juan Santos, Josh Kuperman, and Anders Dale. PROMO: real-time prospective motion correction in MRI using image-based tracking. *Magnetic Resonance in Medicine*, 63(1):91–105, 2010.
- Jennifer L Whitwell. Voxel-based morphometry: an automated technique for assessing structural changes in the brain. *Journal of Neuroscience*, 29(31):9661–9664, 2009.
- Medha V Wyawahare, Pradeep M Patil, Hemant K Abhyankar, et al. Image registration techniques: an overview. *International Journal of Signal Processing, Image Processing and Pattern Recognition*, 2(3):11–28, 2009.
- Xiao Yang, Roland Kwitt, and Marc Niethammer. Fast predictive image registration. In *Deep Learning and Data Labeling for Medical Applications*, pages 48–57. Springer, 2016.
- Xiao Yang, Roland Kwitt, Martin Styner, and Marc Niethammer. Quicksilver: Fast predictive image registration—a deep learning approach. *NeuroImage*, 158:378–396, 2017.
- Sean I Young, Yaël Balbastre, Adrian V Dalca, William M Wells, Juan Eugenio Iglesias, and Bruce Fischl. SuperWarp: Supervised Learning and Warping on U-Net for Invariant Subvoxel-Precise Registration. In *Biomedical Image Registration*, pages 103–115, Cham, 2022. Springer. ISBN 978-3-031-11203-4.
- Evan M Yu, Alan Q. Wang, Adrian V Dalca, and Mert R. Sabuncu. KeyMorph: Robust Multi-modal Affine Registration via Unsupervised Keypoint Detection. In *Medical Imaging with Deep Learning*, 2022.
- Amy Zhao, Guha Balakrishnan, Frédo Durand, John V. Guttag, and Adrian V. Dalca. Data augmentation

- using learned transforms for one-shot medical image segmentation. *Proceedings of the IEEE/CVF Conference on Computer Vision and Pattern Recognition*, abs/1902.09383, 2019a.
- Shengyu Zhao, Yue Dong, Eric I Chang, Yan Xu, et al. Recursive cascaded networks for unsupervised medical image registration. In *Proceedings of the IEEE/CVF International Conference on Computer Vision*, pages 10600–10610, 2019b.
- Shengyu Zhao, Tingfung Lau, Ji Luo, I Eric, Chao Chang, and Yan Xu. Recursive Cascaded Networks for Unsupervised Medical Image Registration (ICCV 2019), 2019c. URL <https://github.com/microsoft/Recursive-Cascaded-Networks>.
- Shengyu Zhao, Tingfung Lau, Ji Luo, I Eric, Chao Chang, and Yan Xu. Unsupervised 3D end-to-end medical image registration with volume tweening network. *IEEE Journal of Biomedical and Health Informatics*, 24(5): 1394–1404, 2019d.
- Zhenyu Zhu, Yiqin Cao, Chenchen Qin, Yi Rao, Di Lin, Qi Dou, Dong Ni, and Yi Wang. Joint affine and deformable three-dimensional networks for brain MRI registration. *Medical Physics*, 48(3):1182–1196, 2021.
- Fuzhen Zhuang, Zhiyuan Qi, Keyu Duan, Dongbo Xi, Yongchun Zhu, Hengshu Zhu, Hui Xiong, and Qing He. A comprehensive survey on transfer learning. *Proceedings of the IEEE*, 109(1):43–76, 2020.

Supplementary material

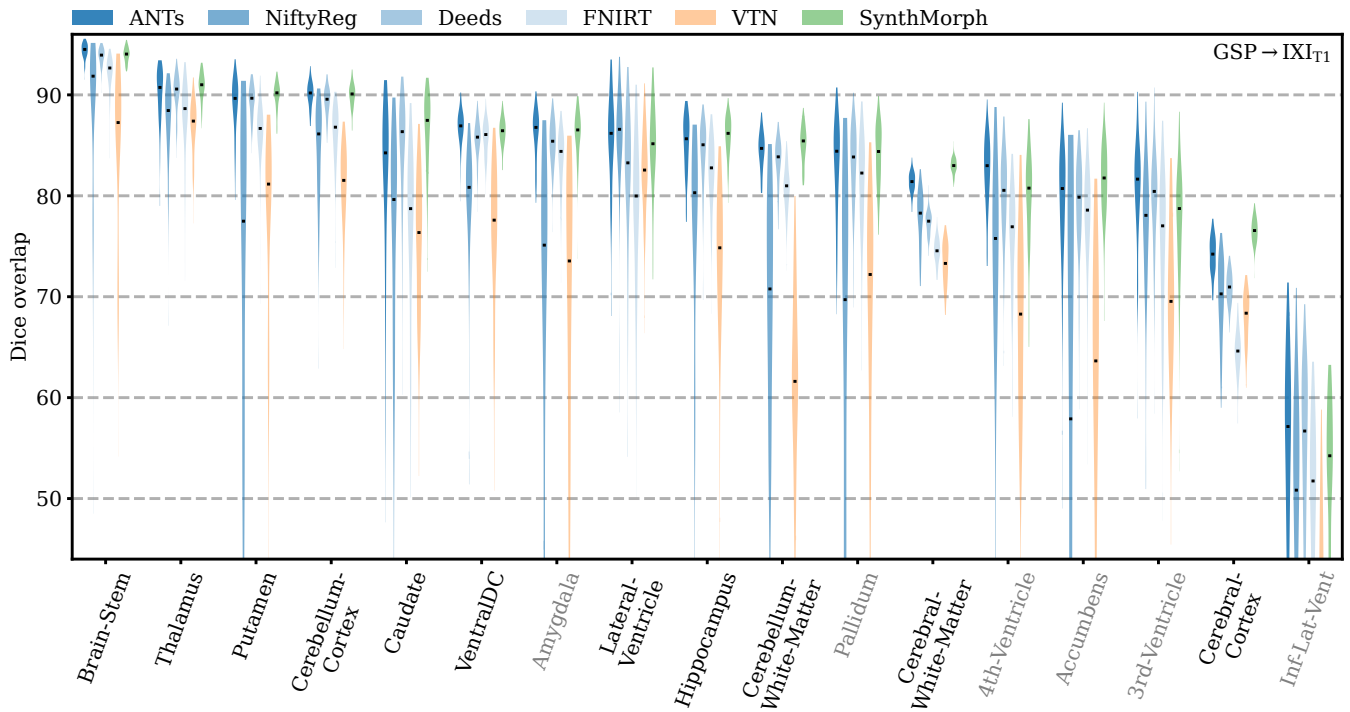


Figure S.1. Deformable 3D registration accuracy per region after affine initialization with NiftyReg. We left-right averaged bilateral brain regions. SynthMorph training did not optimize the overlap of grayed-out regions.

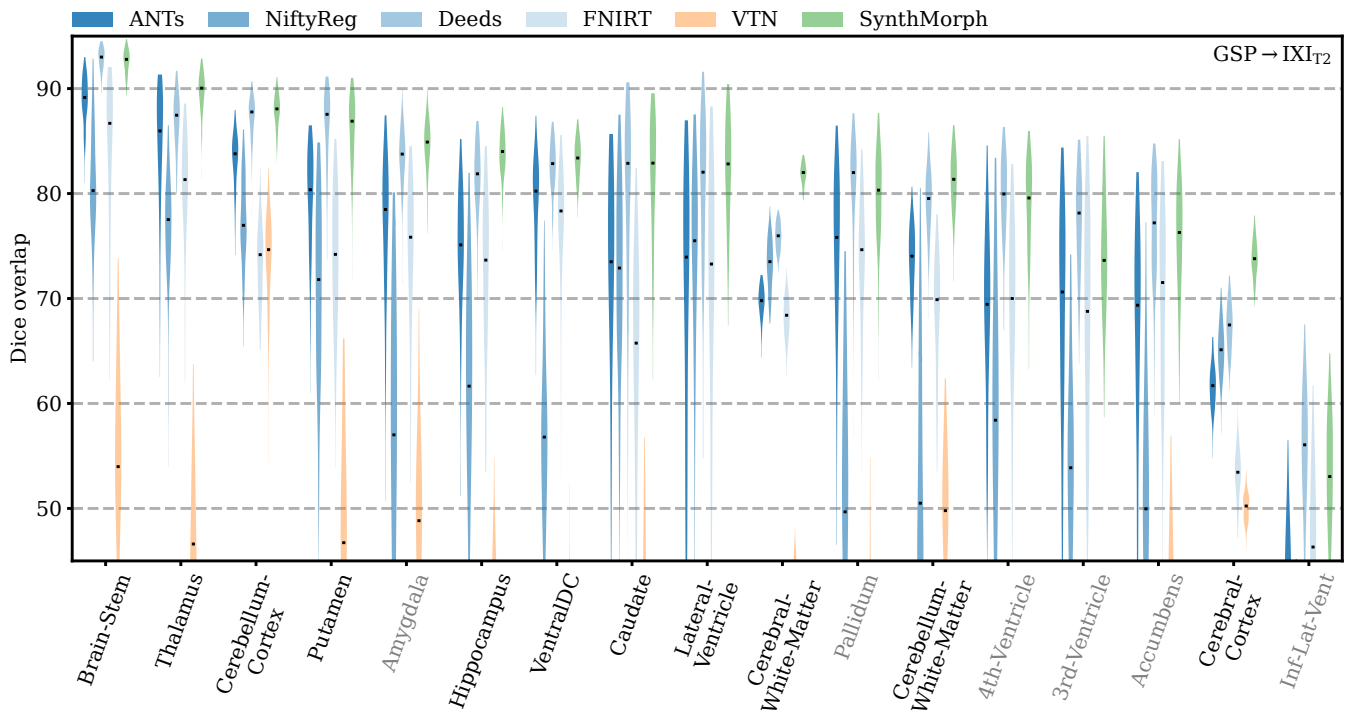


Figure S.2. Deformable 3D registration accuracy per region after affine initialization with NiftyReg. We left-right averaged bilateral brain regions. SynthMorph training did not optimize the overlap of grayed-out regions.

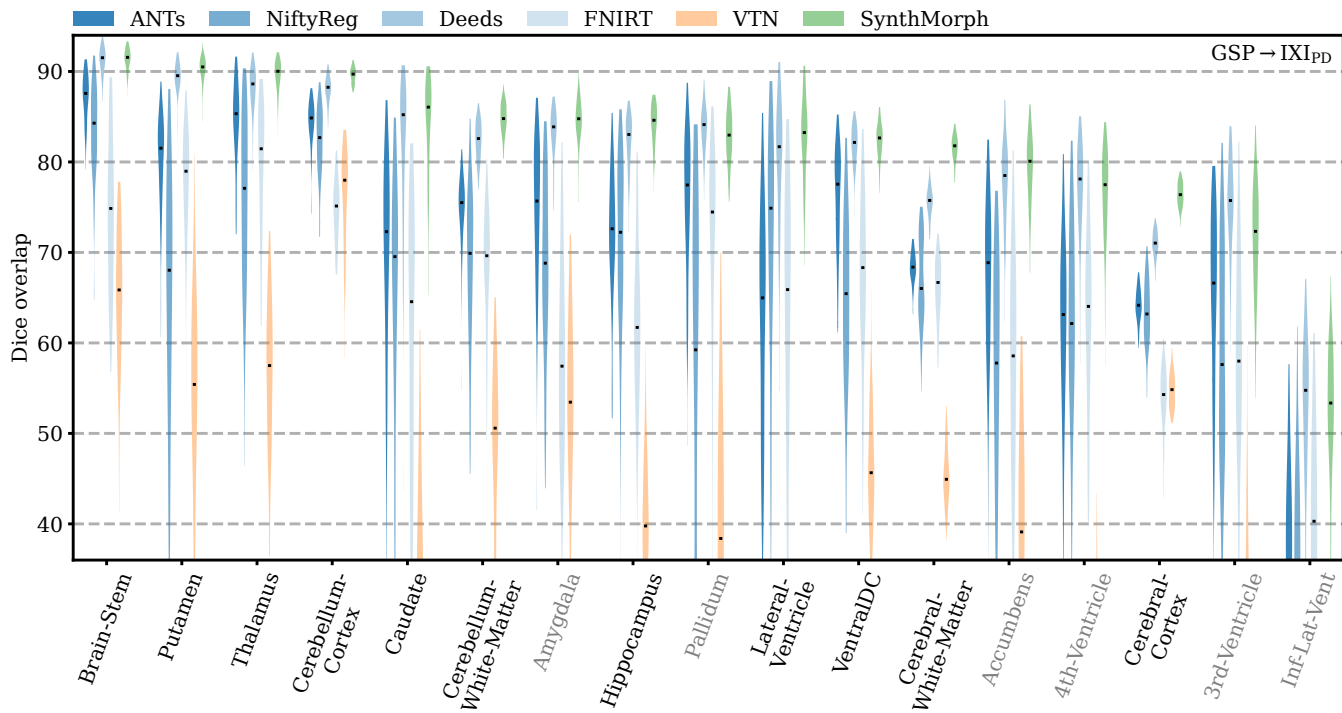


Figure S.3. Deformable 3D registration accuracy per region after affine initialization with NiftyReg. We left-right averaged bilateral brain regions. SynthMorph training did not optimize the overlap of grayed-out regions.

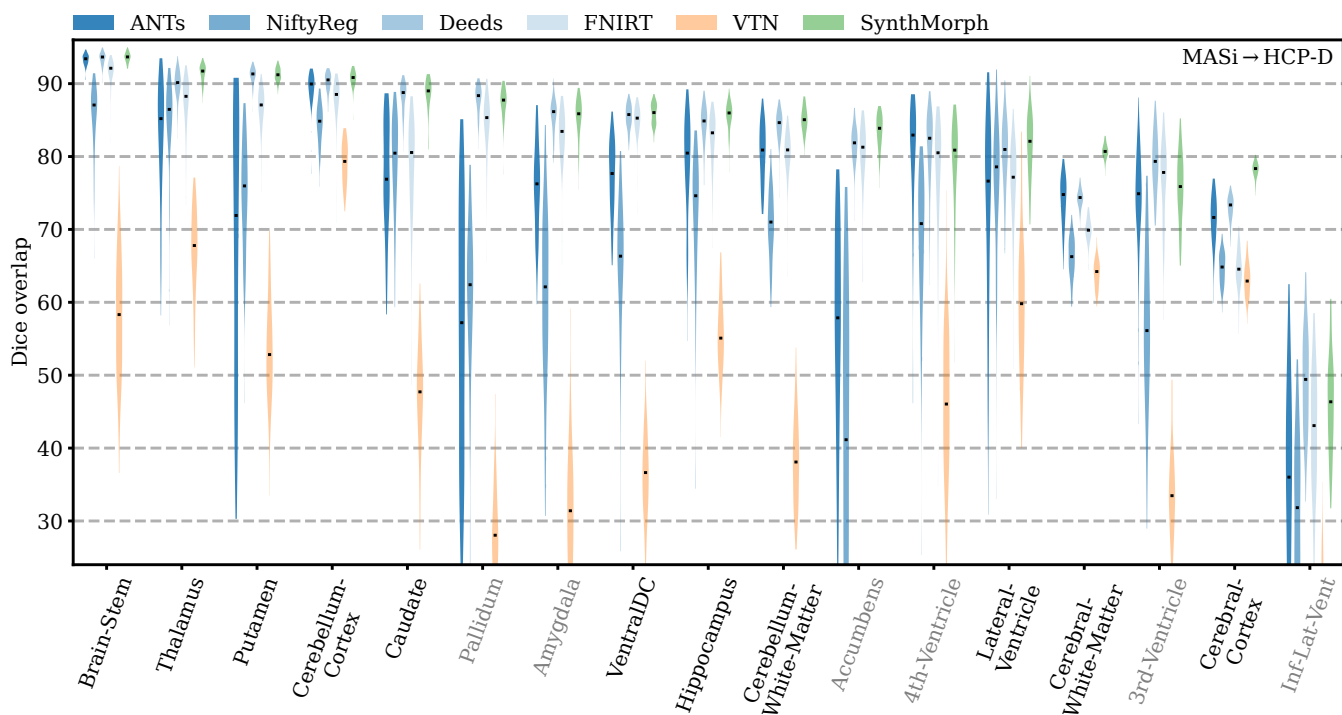


Figure S.4. Deformable 3D registration accuracy per region after affine initialization with NiftyReg. We left-right averaged bilateral brain regions. SynthMorph training did not optimize the overlap of grayed-out regions.

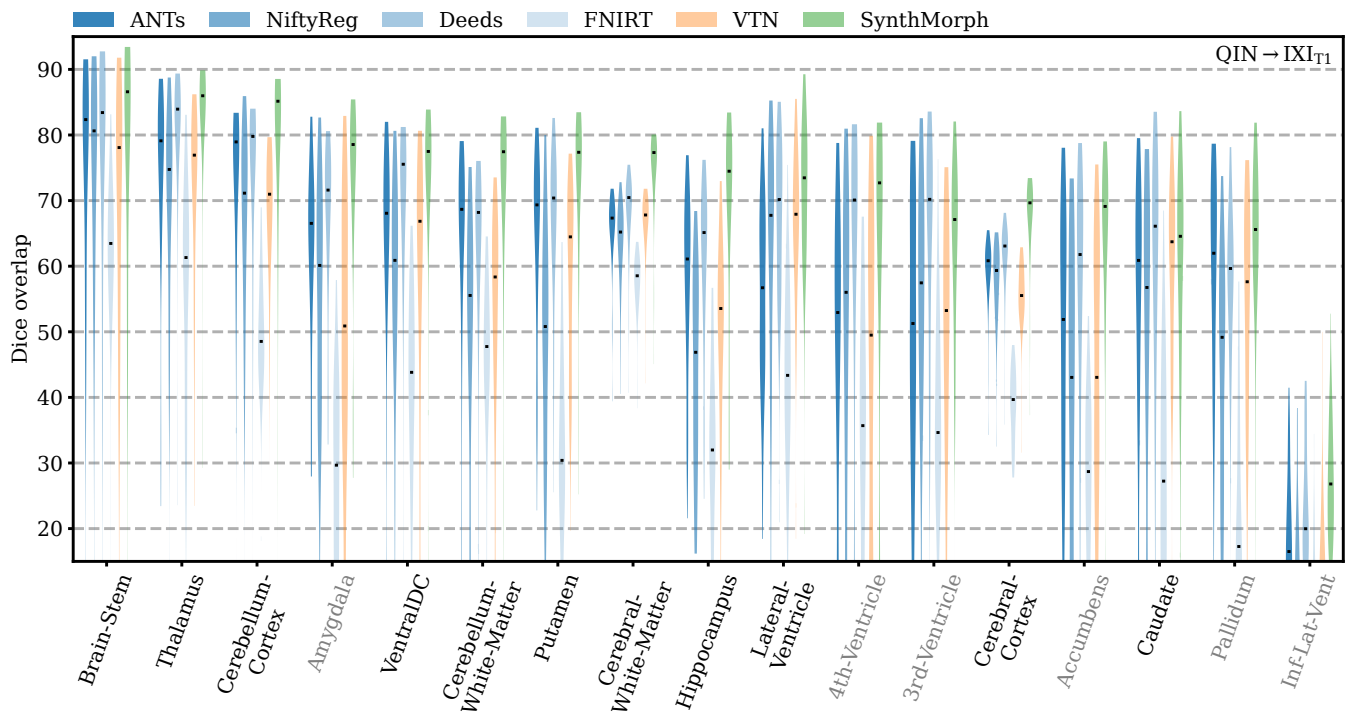


Figure S.5. Deformable 3D registration accuracy per region after affine initialization with NiftyReg. We left-right averaged bilateral brain regions. SynthMorph training did not optimize the overlap of grayed-out regions.